Small impact craters on Mars studied by numerical models and observations at the NASA InSight landing site

Kristina Gilje

Thesis submitted for the degree of
Master of Science in Geosciences
60 credits

Centre for Earth Evolution and Dynamics
Department of Geosciences
Faculty of Mathematics and Natural Sciences

UNIVERSITY OF OSLO
Spring 2019

Small impact craters on Mars studied by numerical models and observations at the NASA InSight landing site

Kristina Gilje

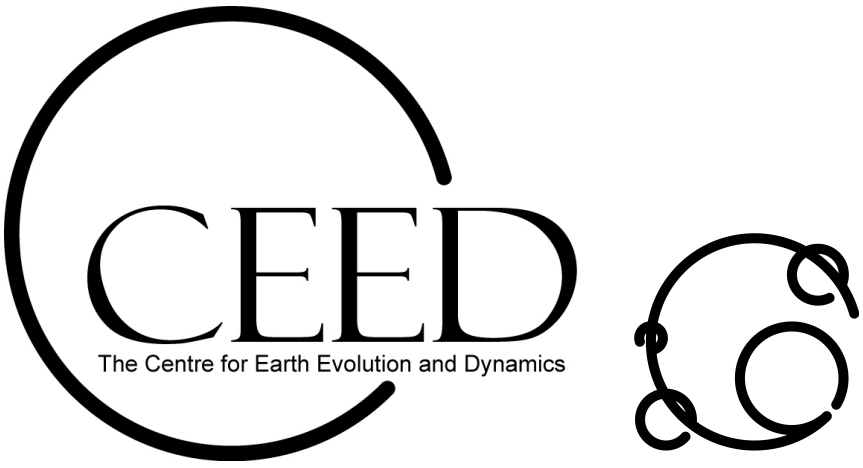

© 2019 Kristina Gilje

Impact cratering on Mars

Supervisors: Prof. Stephanie Werner and Dr. Nils Charles Prieur

http://www.duo.uio.no/

Printed: Reprosentralen, University of Oslo

Abstract

Impact craters are a common geological feature found on a variety of planetary bodies throughout the Solar System and can reveal information about the history of the Solar System and its planets. Specifically, crater statistics can be used in age determination of planetary surfaces, and is currently the only tool available for such purposes. The calibration of the so-called cratering chronology models, from dated lunar samples and size-frequency distribution (SFD) makes it possible to derive more accurate absolute model ages for other planetary surfaces, including Mars. There are several processes that can alter the SFD, and one of them is target properties and this is especially apparent for craters in a smaller diameter range. Several studies have found that target properties, such as porosity, strength, cohesion, and friction play a major role on the final crater diameter size, but todays knowledge is limited.

In this study, a combination of numerical modelling and crater statistics was used to examine the effects of target properties (impact velocity and material) of small craters near the InSight landing site on Mars. The numerical simulations were conducted using the hydrodynamic code iSALE and in total, 128 models were computed for four different velocities and two different target materials, weak material (sand) and harder material (rock). The two model setups was selected based on THEMIS thermal data in the study area were areas with weak material (thought to be dust or sand) and rock, both basaltic in composition, were selected. This study shows that the impact velocity does change the final crater diameter, as expected from crater scaling laws. This is also the case between the two materials tested. While, for the lowest velocity tested (near the lower threshold of subsonic velocity) it fails to obey the expected power law relation between crater size and impactor diameter. In addition, cratering statistics and derivation of crater SFDs were performed for two areas with different target properties for the study area. The crater SFD show that the areas had the same age within the uncertainty, but had several changes in the slope, which could be a result of geological processes or human errors when conducting the crater counting. While, the coupling of the crater SFD with power-laws derived from the numerical models show that the change in slope of the two crater SFDs can possibly be explained by difference in target properties between the areas.

Acknowledgements

I would like to thank my main supervisor, Prof. Stephanie Werner for letting me study impact cratering on such a cool planet as Mars. And for all the feedback I received that improved this thesis.

A spacial thank you to Dr. Nils Prieur for teaching me so much about craters and for all the help I got. Also, thank you to Benjamin Butel for showing me how crater counting works, and for the feedback received.

I would also like to thank my fellow students in the master room at CEED for being such fun people, I am pretty sure that I have acquired more smiling wrinkles during the last two years (which is a good thing). For Rebecca, thank you for being such a good friend and for all the "bookclubes" and nerdy conversations we have had. For Michael, thank you for your support, selflessness, and all of the "bad" jokes which made the master student life better.

Lastly, thank you to my parents and brothers for always being supportive.

Contents

List of Tables

List of Figures

Chapter 1

Introduction

1.1 An introduction to impact cratering and surface age determination

Impact craters are in their simplest form a bowl-shaped depression on a surface and are one of the most fundamental geological features found throughout the Solar System. Craters cover the surface of the terrestrial planets, moons and other solid objects, and are therefore key features in understanding the past history in our Solar System. Impact craters can unveil information of the evolution of the Solar System, but most importantly be used for remote age determination of surfaces (Öpik, 1960; Shoemaker, 1961). Impact craters are the result of a complex sequence of geological processes when an object, either an asteroid or comet, collides with a surface. For planetary bodies in the inner Solar System, most collisions surpass the speed of sound (hypervelocity impact), releasing a massive amount of energy. For example, the Barringer Crater (also called Meteor Crater) in Arizona, USA, was caused by an impact about 50,000 years ago releasing an energy equivalent to 2.5 megatonnes of TNT, which is ~ 150 times the energy released by the Hiroshima bomb (Melosh and Collins, 2005).

The Moon is often the object of choice when studying impact cratering in the Solar System for several reasons. In contrast to Earth, the Moon has experienced low geological activity for the last three billion years. A large number of craters accumulated over this period and can therefore be used to retrace the Solar System history (Robbins, 2017). Moreover, cratering statistics is eased by the fact that the Moon lacks an atmosphere, so that the lunar impact craters erode very slowly over the course of millions to hundreds of millions years. At last, our neighbouring moon is the only planetary body where several rock samples have been dated and compared to crater densities, allowing for the calibration of the projectile impact rate for the Solar System (Neukum and Hiller,

1981).
The density of craters on a surface, binned by size, is used to produce a crater size-frequency distribution (SFD), which in turn are used for age determination, where an area with a larger density of impact craters is expected to be older (Öpik, 1960). Cratering chronology models link crater density and isotopic ages, and as such crater SFD measurements can then be translated to absolute ages rather than only providing a relative sequence of events.
For other planetary bodies direct radiometric dated samples do not exist, neither from returned samples nor from meteorites, because the source for the latter is usually unknown. Thus, the Moon's record remains the only crater and sample record for which reliable cratering chronology models are derived. The lunar record has traditionally been transferred to Mars based on impact rate differences and scaling laws (Ivanov, 2001). In recent years, more studies have focused on Mars to check the transfer from the Moon to Mars and the Solar System evolution models. Recently, new models look at a possible link between martian shegottite meteorites and its source crater, the Mojave crater (Werner et al., 2014). Martian in-situ measurements of cosmic ray exposure and K-Ar ages from the Curiosity rover from Farley et al. (2014) were used to constrain the martian cratering chronology model. The future of the models will be augmented by: (1) mars sample return (e.g., NASA Mars 2020, Beaty et al., 2015) and (2) to improve scaling laws for Mars, this is important, because Mars has more variability of terrain than the Moon. Sample return can ensure better calibration for Mars chronology models (currently calibrated from the lunar record) and is imperative to assure satisfactory chronology models for other planetary bodies (Ivanov, 2001).
Therefore, the study of target property influence on the crater scaling laws between different planetary bodies is one of the key issues, to test the variability of crater chronology models.

There still exist several issues and challenges in using cratering statistics as an age determination method, one of them is the influence of target properties on the final crater size (Williams et al., 2018). When considering targets of different strength, an impactor with the same impact velocity and size will produce a larger crater in the weaker target (Melosh, 1989). If not properly accounted for, target properties can result in a difference in absolute ages. Therefore, it can lead to erroneous conclusions when reconstructing the history of a planetary surface. For young surfaces this is especially important, as only small craters are available. Small craters are also more influenced by target properties and knowing more about the influence of target properties will also help greatly in quantifying the contamination by secondary impacts.

1.2 Objectives and motivation

To improve the chronology model and thus get better age constraints for the Moon and other terrestrial bodies, more knowledge is required. Especially regarding improved crater statistics by more precise characterisation of the surfaces and high resolution images. Also important is the assessment of the crater scaling laws by numerical modelling of the impact process and morphological studies. In this work, the main goal is to investigate the influence of target properties and impact velocity, by coupling numerical modelling and crater statistics. For the numerical experiments, the effects of target properties and impact velocity are tested by using two different materials, weak and hard material, and for four different velocities. Crater statistics are performed using SFD measurements. This is especially needed for smaller, simple craters with a diameter less than approximately 1 km, as they are more numerous and can be used to date young surfaces (Werner and Ivanov, 2015). Moreover, small craters are also more susceptible to depositional and erosion processes that obliterate small craters (Werner, personal communication). For simple craters final crater size depends on physical properties of the target and whether strength or gravity is the governing regime in limiting the size (Holsapple, 1993).

The study area is located near the landing site of the InSight (Interior Exploration using Seismic Investigations, Geodesy and Heat Transport) lander in the southwestern part of Elysium Planitia on Mars. Elysium Planitia is the second largest volcanic province on Mars after Tharsis (Werner, 2009), and both weak (sand) and hard-type targets have been detected from THEMIS (Thermal Emission Imaging System) infrared images (Golombek et al., 2017) in this region. The two different targets may have formed at the same time, and therefore this area is a good candidate to investigate the influence of target properties on cratering statistics.
The InSight mission features a robotic lander that will, in addition to other experiments, measure marsquakes by using a seismometer to get a better understanding of the interior structure of Mars (Panning et al., 2017). The marsquakes could also be caused by small impacts, with the potential to provide useful information about formation frequency of small craters, but also possibly to establish a link between impact energy and seismic energy. Numerical modelling of small impact craters could therefore prove to be important in the future.

1.3 Outline

This thesis feature two main methods, numerical modelling and crater statistics. The background theory chapter contains descriptions of the impact formation process, the resulting crater morphology and crater scaling laws important for the presented study. Further, the method used for the numerical modelling and crater counting are separated in two chapters. The crater counting chapter also includes brief background theory of the topic. The results chapter is divided into three sections: one for numerical modelling, then the results from the crater counting and finally the coupling of both. The discussion will also be divided into three parts, numerical modelling, followed by crater counting and lastly the coupling of both. Lastly, a summary of major findings and future work is presented.

Chapter 2

Theoretical background

2.1 Crater mechanics: The three stages of crater formation

When an impactor, asteroid or comet, collides with a solid surface, several mechanisms set in place to form an impact crater. The impact event is usually described in three stages: contact and compression, excavation, and the modification stage (Gault et al., 1968; Melosh, 1989). Each stage is associated with different physical processes, and the division makes it easier to describe the mechanisms behind the formation of impact craters. The formation process for simple impacts is summed up in Figure 2.1 and for complex craters in Figure 2.2. Below is a description of each of the stages, including the main mechanisms.

2.1.1 Contact and compression stage

The contact and compression (Figure 2.1(a) and (b)) stage starts at first contact between the impactor and a solid planetary surface, and is the fastest of the three stages (Melosh, 1989). It is the same for both simple and complex craters. The impactor decelerates and thus compresses at a rapid rate and kinetic energy is transferred to the rocks below (Melosh, 2013). It is during this compression of the impactor and target that two shock waves are created; (1) one shock wave propagates through the impactor from the contact point and refracts when it reaches the boundary of the impactor, (2) the other shock wave travels into the target and subsequently damages the rocks (Melosh, 1989; Collins et al., 2012). The pressure and temperature conditions increases dramatically during the compression, far exceeding the strength of the target and impactor (Collins et al., 2012), causing a zone of damaged and shock metamorphosed rocks. When the refracted wave (also called release wave) from the impactor travels downward towards the target, the high pressure is released and can cause the impactor to completely va-

porise or melt (Melosh, 1989). This decompression marks the end of the contact and compression stage.

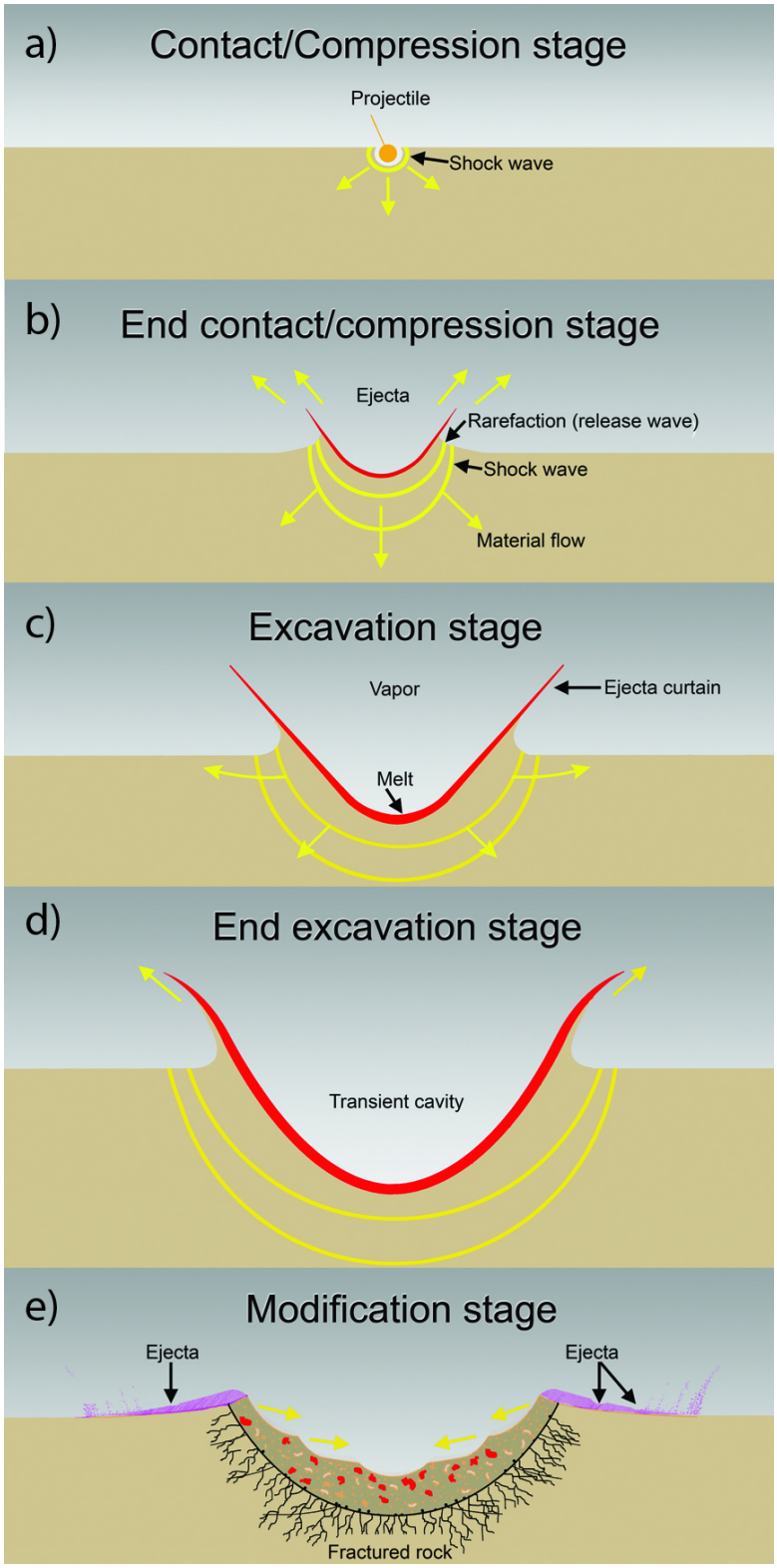

Figure 2.1: Simple impact crater formation: a) and b) contact and compression, c) and d) excavation and e) modification as described in the text (modified after Bevan M. French/David A. Kring/LPI/UA)

2.1.2 Excavation stage

Following the contact and compression stage is the excavation stage (c) and d) in Figure 2.1 and a) and b) in Figure 2.2) where the material is displaced and the crater cavity starts forming. The combination of shock- and refraction waves created in the first stage creates motion in the target rock, causing material to move along excavation flow lines away from the impact site (Osinski et al., 2013). During excavation, the uppermost material of the target is ejected out of the crater cavity. The ejected material will spread out and form an ejecta blanket, which is thickest at the crater rim and pinching out and extending up to one crater diameter away from the rim (Osinski et al., 2013). Continuing the excavation of the crater cavity, at one point it reaches the maximum volume of excavated material during the crater formation process, which is called the transient crater (Dence et al., 1977). Further, when the shock and refracted wave propagates radially in the target it diminishes to stress waves as the energy decreases and the distance from the impactor increases (Melosh, 1989). The excavation stops when the velocity of the excavation flow is no longer high enough to overcome gravity (Osinski et al., 2013) or the strength of the target (Kenkmann et al., 2012), marking the end of the excavation stage.

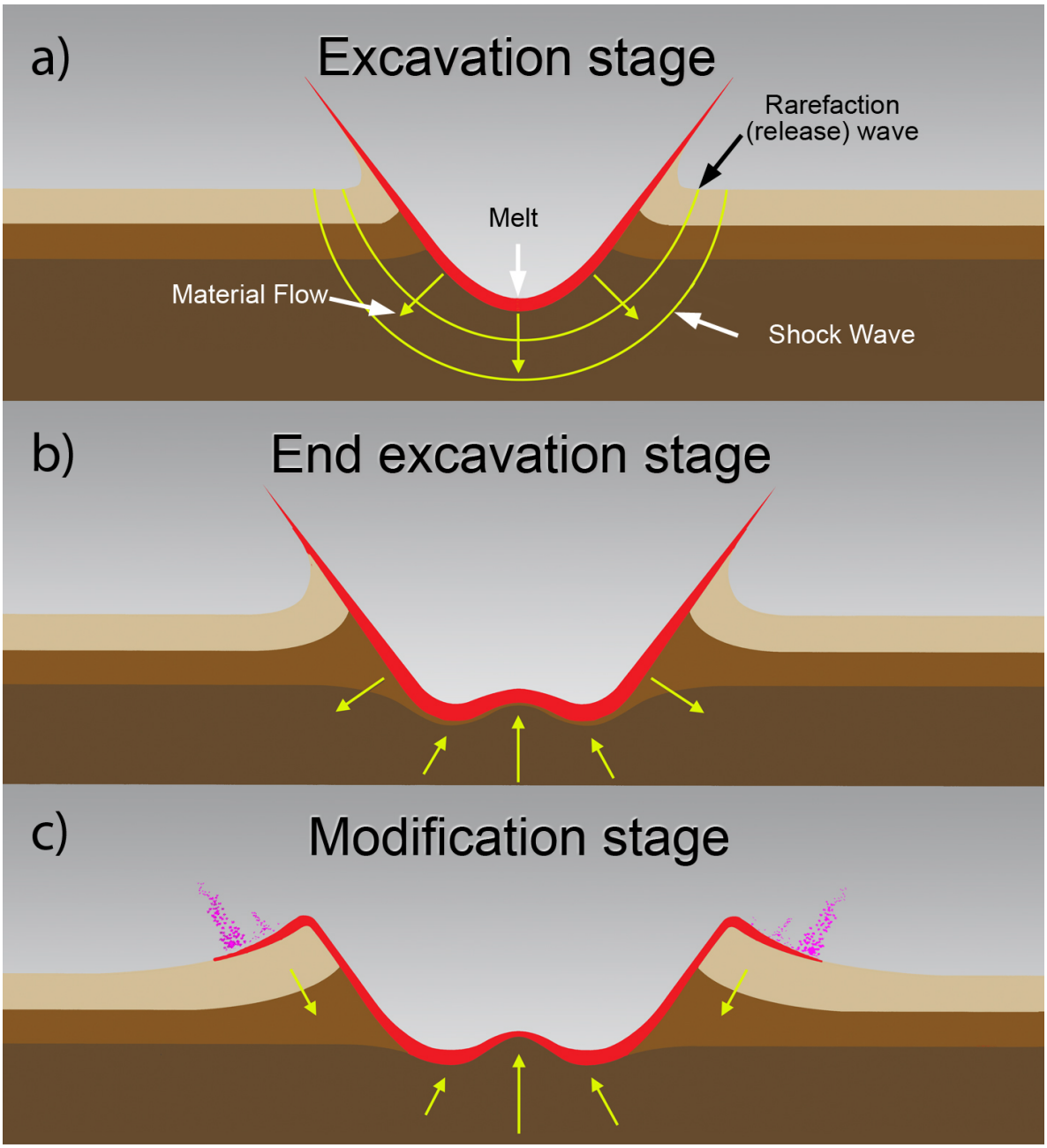

Figure 2.2: Complex impact crater formation: a) and b) excavation and c) modification as described in the text (modified after Bevan M. French/David A. Kring/LPI/UA)

2.1.3 Modification stage

The modification stage describes the transition from the transient crater to the final crater and is the last stage in the impact crater formation. During this stage the evolution to the final crater is different for simple and complex craters. The bowl-shaped simple craters are formed when unstable material of the transient crater begins to slide down the crater walls (Melosh, 1989) ((e) in Figure 2.1). This results is a final crater that is shallower than the transient crater.

For complex craters, the elastic rebound (i.e. uplift) of the transient crater floor is the responsible mechanism for creating the characteristic central peak (Melosh and Ivanov, 1999) ((c) in Figure 2.2). However, if the transient crater is large enough the central uplift peak will collapse and instead creating a peak ring (Melosh, 1989). The central peak formation can be compared to a droplet hitting water and creating a central jet. Melosh (1979) introduced the concept of acoustic fluidization, in which the shock of the impact itself can create vibration in the debris causing the rocks to briefly behave as a Newtonian fluid.

2.2 Crater morphology

Impact craters can be distinctly categorised into three main groups: Simple craters, complex craters and multi-ringed basins. This division is based on the morphology of the craters, where each group has different characteristics. The interior morphology gets increasingly more complex (hence the name complex craters) as the size of the crater increases, due to the amount of gravitational instability, fluidisation, and collapse that occurs during the modification stage (Melosh and Ivanov, 1999). Also, important to note that the amount of modification a crater undergoes is heavily influenced by the properties of the target and the gravity of the planet on which the crater is formed (Melosh and Ivanov, 1999). Below is a summary of the three main crater groups with emphasis on the simple craters as these are the most relevant for this thesis.

2.2.1 Simple craters

Simple impact craters are circular bowl-shaped depressions with steep interior walls (slope of $\sim 25 - 30°$) featuring a lens of brecciated material with fractured bedrock underneath (Pike, 1977; Melosh and Ivanov, 1999) (Figure 2.3). The breccia lens is formed when fractured and melted material move from the transient crater walls downward into the crater. This forms a mixture of material with melt-rich inclusions where the breccia lens is almost as thick as the final crater depth in the centre of the crater (Werner and Ivanov, 2015). Due to uplift during the formation process and the emplacement of the ejecta, simple craters also feature an elevated rim. The height of the rim compared to the surrounding topography is approximately 4% of the diameter of the crater (Melosh, 1989). For typical, unaltered, simple craters the final depth to diameter ratio is approximately 1/5 (Melosh, 1989).

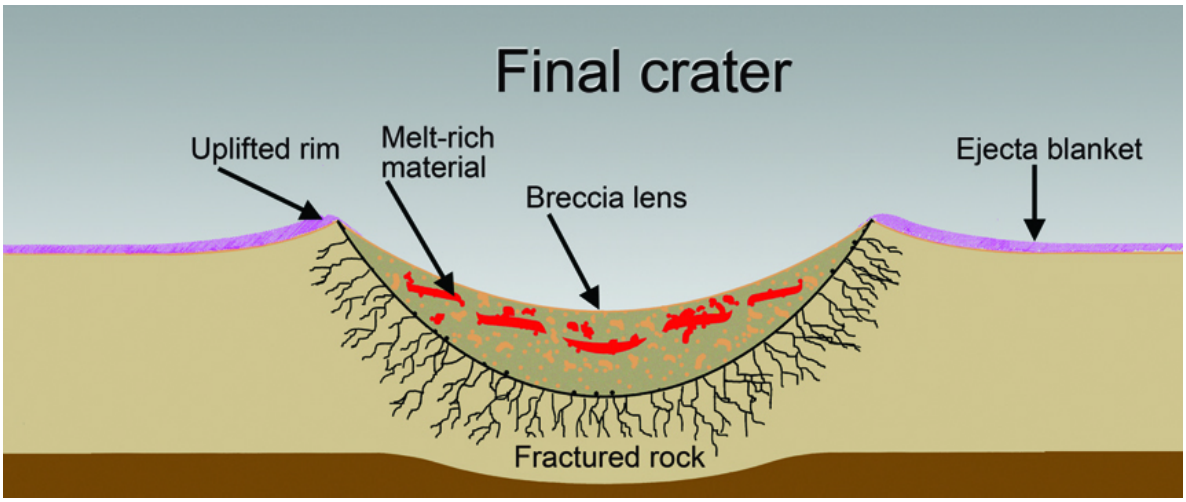

Figure 2.3: Cross-section of a final simple crater showing key features (Illustration credit: Bevan M. French/David A. Kring/LPI/UA).

However, the morphology of simple craters changes if the target is layered and has different strength and/or impact velocity (Prieur et al., 2018). Then three additional simple crater morphologies can be described: (1) central mound, where large parts of the upper layer slump down into the crater due to low strength, (2) flat-bottomed, where the simple crater features a flat floor due to increased strength contrast between the layers (or lower impact velocity) so that the upper layer decouples from the lower layer, and (3) concentric simple craters where the two layers decouple to form a step in the wall between the layers due to strength contrast (Prieur et al., 2018). Figure 2.4 features images of the four different simple crater morphologies from the Moon, where such morphologies are common.

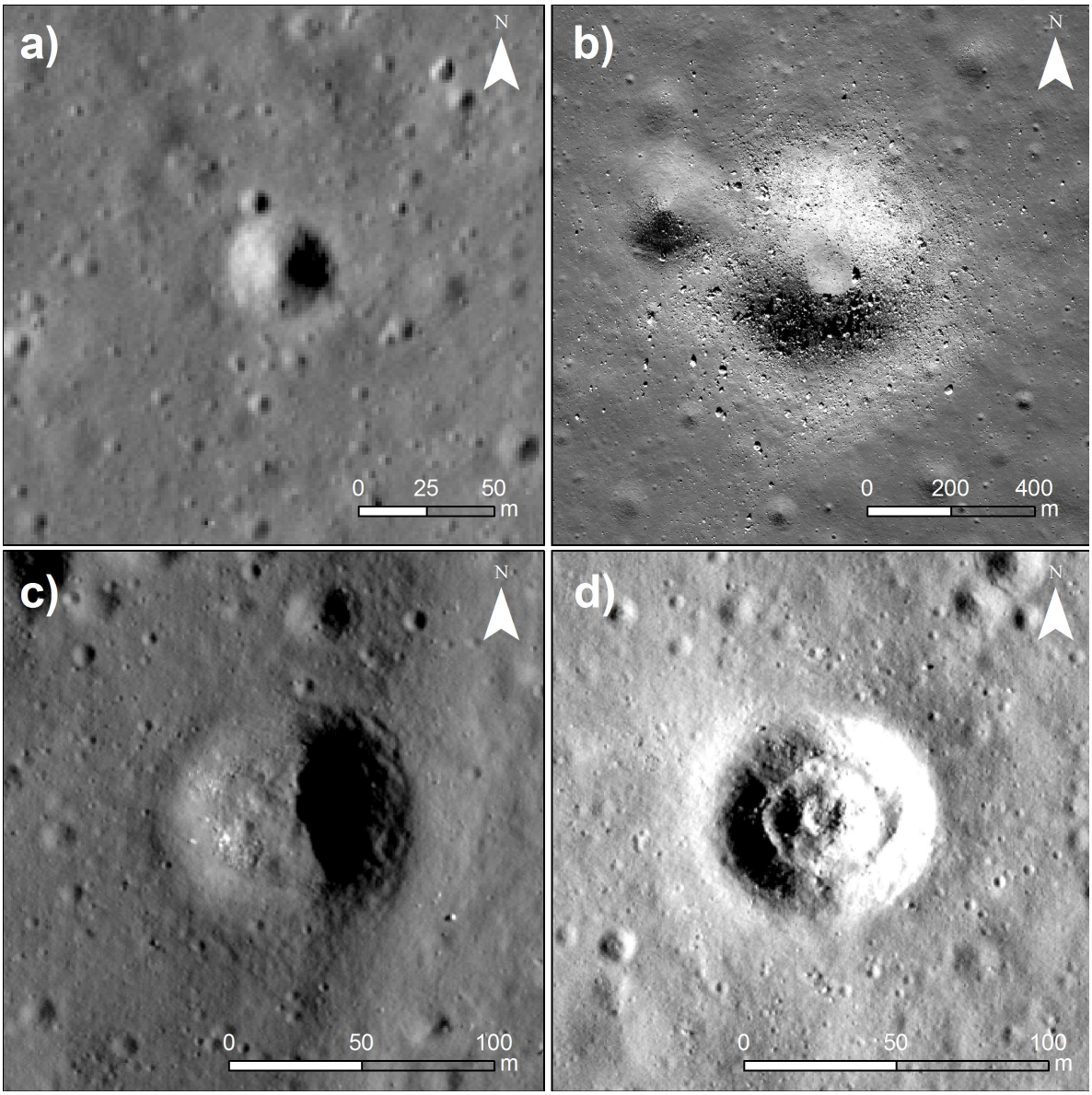

Figure 2.4: Different simple crater morphologies on the Moon: a) normal bowl-shaped, b) central-mound, c) flat-bottomed, d) concentric. Figure is from Prieur et al. (2018).

2.2.2 Complex craters

The size at which the transition from simple to complex craters occurs is different for each planetary body, and the final crater morphology depends on the surface gravity of the body (Melosh, 2011). This relationship is scaled by the inverse of gravity, $1/g$, which determines at which diameter the transition occurs (Melosh and Ivanov, 1999). This means for planets with higher surface gravity, the transition will occur at a smaller crater diameter. The transition on Earth happens at 2-4 km diameter, while on the Moon at about 15-20 km and on Mars 5-10 km (Pike, 1988; Melosh and Ivanov, 1999). Complex craters have undergone a more complicated modification stage than simple craters resulting in a crater morphology that consist of several characteristic features

(Figure 2.5). The first apparent feature is the presence of a central peak. The outer walls of the complex crater are terraced by normal faults dipping toward the centre of the crater. Inbetween the central peak and the terraced walls is a flat floor, in which the breccia and melts can be found. The complex craters are usually shallower than the simple craters, with a depth-to-diameter ratio lower than 1/5 depending on diameter (Pike, 1977). Figure 2.5 shows the complex crater morphology.

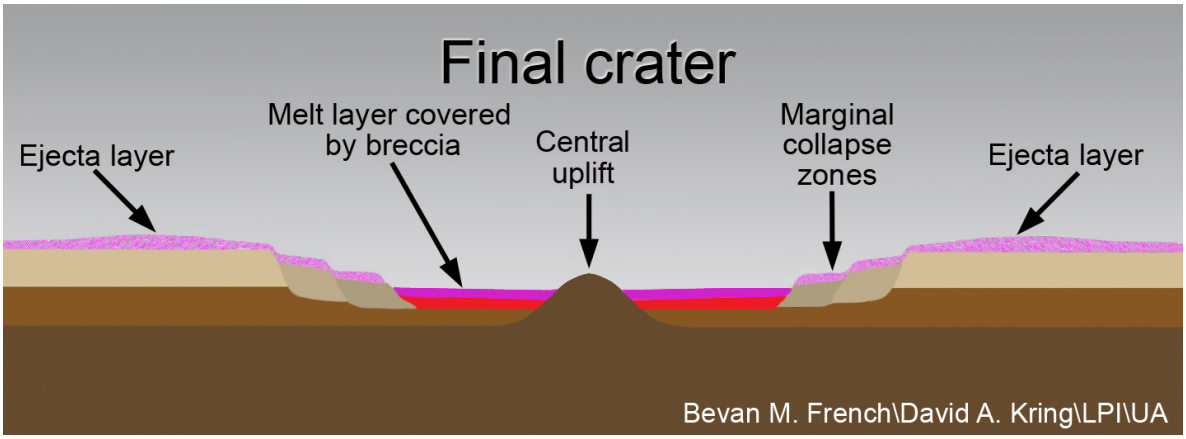

Figure 2.5: Cross-section of a final complex crater showing key features (Illustration credit: Bevan M. French/David A. Kring/LPI/UA).

2.2.3 Multi-ringed basins

Multi-ring basins are the largest crater type and, as the name states, consist of one or more rings (Osinski and Pierazzo, 2013). There are two types of multi-ring basin morphologies, exemplified by craters on the Moon and the Jovian satellite Callisto. The Orientale Basin on the Moon is about 900 km in diameter and features at least three rings facing inwards and the elevation is increasing with each ring. The other type is derived from the 3000 km in diameter large basin Valhalla on Callisto. This type features not only a few rings, but up to hundreds, which are more closely spaced than in the Orientale type (Osinski and Pierazzo, 2013). The rings are facing outward from a flat central basin. It is important to note that these rings are not the same as central rings formed in complex craters, as the multi-rings are not formed inside the final crater (Melosh, 1989; Osinski and Pierazzo, 2013).

2.3 Crater scaling laws

Scaling laws are used to predict the size (depth, diameter and volume)(Holsapple, 1993) of craters based on the properties of the impactor and target (Prieur et al., 2017), but can be used to get a better understanding of the crater formation process. Also, it gives the opportunity to compare small craters produced in a laboratory setting with large

natural craters where the projectile size is very different (Elbeshausen et al., 2009). There are thus several variables to take into account related to the impactor: (1) impact angle, (2) velocity, (3) projectile size and (4) density. Note that the scaling laws in this section are for vertical impacts, and therefore the impact angle is not included in the equations. In addition, to have an understanding of the geology of the target is crucial as it will have an effect on the final crater size and morphology. The physical properties of the target include: (1) strength as a function of cohesion, porosity and friction, (2) density, (3) layering and (4) gravity of the respective planetary body. Stratigraphy is also important as multiple layers of rocks with different densities will affect the morphology of the final crater (Piekutowski, 1977; Senft and Stewart, 2007).

The fundamentals for scaling laws is the point source theory, where an impact can be approximated by a single point that is buried at a certain depth. This point is the source of energy and momentum, and is transferred to the target in a small area called the coupling zone (Dienes and Walsh, 1970; Holsapple and Schmidt, 1987; Schmidt and Housen, 1987). The coupling zone needs to be smaller than the transient crater size in order for the point-source approximation to be valid, and thus only far-field processes can be described by this method. If the point-source approximation criteria is fulfilled then the energy and momentum transfer can be described by the coupling parameter C (Eq. 2.1), which depends on the impactor diameter L, velocity U and density δ (Schmidt and Housen, 1987; Holsapple and Schmidt, 1987; Holsapple, 1993):

$$C = L\, U^{\mu}\, \delta^{\nu} \tag{2.1}$$

In Equation 2.1, L is the impactor diameter, U is impact velocity, μ is the velocity-scaling exponent and ν the density-scaling exponent (Holsapple, 1993; Kurosawa and Takada, 2019; Prieur et al., 2017). The value of the exponent μ depends on the physical properties of the target (Holsapple and Schmidt, 1987) and has a lower and upper limit of 1/3 and 2/3 respectively. The lower limit coincides with the momentum scaling and the upper limit to the energy scaling (Dienes and Walsh, 1970; Holsapple, 1993). The density-scaling exponent takes into account the difference in density of the impactor and target material, and is often assumed to be $\nu = 1/3$ for both the energy and momentum scaling (Holsapple, 1993; Kurosawa and Takada, 2019). Impacts with the same C value will produce craters of the same size and can therefore be used to derive power-laws to scale the final crater size to the scaled impact size (Wünnemann et al., 2011).

The most prevalent method for predicting the crater size is the π-group scaling laws (Schmidt, 1980; Schmidt and Housen, 1987; Holsapple, 1993), which is originally formu-

lated from the Buckingham π-Theorem (Buckingham, 1914). This type of dimensional analysis relates a determined set of variables to dimensionless ratios. By this type of scaling the number of variables needed to define either the volume V, diameter D or depth d of the transient crater are reduced from:

$$V, D, d = F\left(U, L, \rho, \delta, Y_{EFF}, g\right) \tag{2.2}$$

where ρ is density of the target, δ is density of the impactor, Y is strength and g is gravity. The dimensionless form of equation (2.2), which contains only non-dimensional variables is as follows:

$$\pi_V, \pi_D, \pi_d = F'\left(\pi_2, \pi_3, \pi_4\right) \tag{2.3}$$

where π_V, is the cratering efficiency (mass of the excavated crater material (ρV) divided by the mass of the impactor (m), see Eq. 2.4) (Wünnemann et al., 2011; Holsapple, 1993), π_d (Eq. 2.5) and π_D (Eq. 2.6) are the dimensionless ratios of depth and diameter:

$$\pi_V = \frac{\rho V}{m} \tag{2.4}$$

$$\pi_D = D\left(\frac{\rho}{m}\right)^{\frac{1}{3}} \tag{2.5}$$

$$\pi_d = d\left(\frac{\rho}{m}\right)^{\frac{1}{3}} \tag{2.6}$$

π_2 (Equation 2.7) is the gravity-scaled size and is a relation between gravitational and inertial stresses (Wünnemann et al., 2011) and expresses the importance of gravity in inhibiting the transient crater growth. If gravity or the size of the impactor increases, the cratering efficiency decreases and thus the transient crater becomes smaller (Holsapple, 1993). The ratio between material strength of the target and the initial dynamic pressure (ρU^2) also inhibit crater growth and is expressed by the non-dimensional strength-scaled size π_3 (Wünnemann et al., 2011; Holsapple, 1993). In π_3 (Equation 2.8) the overall strength parameter Y_{EFF} is the summed effect of how the strength of the target material either inhibits or promotes crater growth. The effective strength is a function of physical properties such as friction, porosity and cohesion and how damaged

the material is (Holsapple, 1993; Wünnemann et al., 2011; Prieur et al., 2017). Lastly, π_4 (Equation 2.9) is the ratio of the target and impactor density, which is especially important in laboratory experiments where the impactor properties often are changed in order to reach higher impact velocity.

$$\pi_2 = 1.61\frac{gL}{U^2} \tag{2.7}$$

$$\pi_3 = \frac{Y_{EFF}}{\rho U^2} \tag{2.8}$$

$$\pi_4 = \frac{\rho}{\delta} \tag{2.9}$$

The relationship between the scaling laws derived from dimensional analysis stated above can be validated and verified by laboratory experiments (Holsapple, 1993; Holsapple and Housen, 2007) and/or numerical simulations (Wünnemann et al., 2011).

In this thesis π_D is the most important scaling law to consider. It is proportional to the ratio between the transient crater diameter and the projectile diameter or final rim-to-rim diameter depending on what is of interest, and is a measure of the efficiency of crater growth (Prieur et al., 2017). π_D can be expressed by one dimensionless equation that is valid for both the strength and gravity regime (Holsapple, 1993). By combining equation π_D ,π_2, π_3 and π_4 with the coupling parameter the following equation can be derived (Holsapple, 1993; Kurosawa and Takada, 2019):

$$\pi_D = K_1 \left[\pi_2 \, {\pi_4}^{\frac{2+\mu-6\nu}{-3\mu}} + \left(\pi_3 \, {\pi_4}^{\frac{2-6\nu}{-3\mu}} \right)^{\frac{2+\mu}{2}} \right]^{\frac{-\mu}{2+\mu}} \tag{2.10}$$

where K_1 is a scaling coefficient determined by laboratory experiments or numerical modelling. This is also the case for the exponents μ and ν. Another scaling coefficient K_2 is included in the effective strength parameter Y_{EFF} (Holsapple, 1993).
If π_3 is much larger than π_2, like for rock, so that $Y_{EFF} \neq 0$ and $\pi_3 \neq 0$ then π_3 will be larger than π_2, and the strength regime dominates. Equation 2.10 then becomes:

$$\pi_D = K_1 \, {\pi_3}^{\frac{-\mu}{2}} \, {\pi_4}^{\frac{1-3\nu}{3}} \tag{2.11}$$

But if the strength is negligible (Y=0) and $\pi_3 = 0$, then the gravity regime dominates ($\pi_2 \gg \pi_3$). This is typical for very large craters or granular targets, for example sand (Prieur et al., 2017), and thus equation 2.10 can be reduced to:

$$\pi_D = K_1 \, \pi_2^{\frac{-\mu}{2+\mu}} \, \pi_4^{\frac{2+\mu-6\nu}{3(2+\mu)}} \tag{2.12}$$

Equation 2.12 can be further simplified to:

$$\pi_D = K_D \, \pi_2^{-\beta} \tag{2.13}$$

where

$$K_D = K_1 \, \pi_4^{\frac{2+\mu-6\nu}{3(2+\mu)}} \tag{2.14}$$

and

$$\beta = \frac{\mu}{2+\mu} \tag{2.15}$$

The transition from strength to gravity dominated regimes is transitional, so in nature it might not be a black and white case.

Chapter 3

Impact crater numerical modelling

3.1 Principles of Numerical Modelling - iSALE

Numerical modelling is a reliable tool to be able to study the whole crater formation process as it is rare to observe the whole process happening in real time. It is possible to run simulations that are realistic in terms of size-scale, gravity, impact angle and velocity, and parameters can be tested independently from each other. The hydrocodes must be validated against experiments to assure the accuracy, and iSALE has been extensively tested and validated.

In this master's thesis iSALE-2D (impact Simplified Arbitrary Lagrangian Eulerian) shock physics code (Wünnemann et al., 2006) was used to simulate the impact process. The iSALE code is an extension of the SALE hydrocode (Amsden et al., 1980) and was modified to simulate hypervelocity impacts in solid materials. The extension include an elasto-plastic constitutive model, fragmentation models, several equations of state (EoS), and the possibility for several equations of state (Melosh et al., 1992; Ivanov et al., 1997). Newer improvements to the code include a modified strength model (Collins et al., 2004), a porosity compaction model (Wünnemann et al., 2006; Collins et al., 2011) and a dilatancy model (Collins, 2014).

In two dimensions numerical simulations are limited to vertical impacts, but gives axial symmetry and thus simplify the model. Most impact craters are symmetric in shape for impact angles larger than $\sim 30^{\circ}$ (Gault and Wedekind, 1978; Elbeshausen et al., 2009), this is a reasonable assumption, as it is taken into account that less energy will be transferred to the target by using the vertical component of the impact velocity. Elbeshausen et al. (2009) showed that using the vertical component of an impact angle is reasonable for coefficient of friction for ~ 0.7 or higher, as for sand. This also means that two dimensional modelling will use less computational power than the more realis-

tic three dimensional model. The most probable impact angle in the solar system is 45 degrees (Collins et al., 2013), so in order to take into account the lower energy input, all velocities used in this work are the vertical component of the 45 degree velocity.

The mesh used in iSALE-2D consists of a high resolution zone of constant size and extensional zones above, below and to the right of the high resolution zone (Figure 3.1). The grid sizing of the extensional zone increase with 3% (standard value, but this can be chosen) by each cell to be sure that there will not be any reflection effects (e.g. pressure wave reflections that can potentially influence the crater evolution) at the boundaries of the model. The mesh is fixed in space with the material flowing through the cells (Eulerian description) which means that the code computes a new set of variables for each cell based on how much of the mass, momentum and energy is transferred from the adjacent cell (Collins et al., 2013).

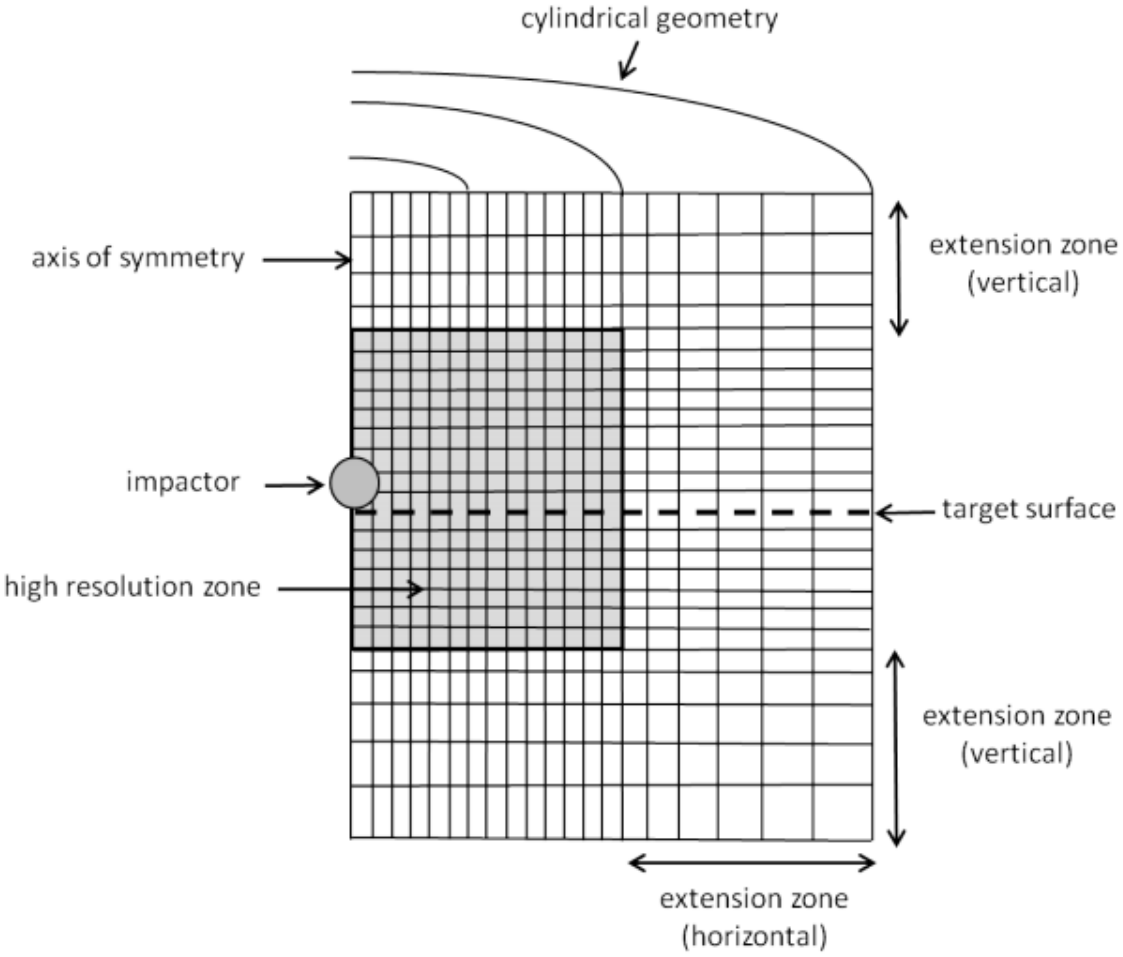

Figure 3.1: The grid used in iSALE features high resolution zone where the craters are formed. Extensional zones is added to the top, bottom and right of this high resolution zone to make sure that no relection on the boundary occur (Figure is from Potter (2012)).

For the boundary conditions of the mesh the default values was used. The right and top boundaries allow outflow of the material, while the left side is free-slip meaning that the material velocity is zero normal to the boundary and the bottom boundary has no slip (e.g. the material has zero velocity relative to the boundary).
The grid size depends on the number of cells per projectile radius (CPPR) which is a parameter that can be chosen. This means that the grid size will be smaller the higher the CPPR and vice versa, and thus affects the resolution of the model. The higher the CPPR, more cells are needed in the high resolution zone, but this also give more accurate results.

3.2 Numerical experiments

In this work, simulations were conducted for the martian surface ($g = 3.711 km/s$) for two different materials: basalt sand and basalt rock. These were used as an analogue for the lava plains (with varying dust cover) in Elysium Planitia, where the basaltic sand is the dust covered areas and basaltic rock the lava plains. For each of the materials four different impact velocities were tested. The different impact velocities are based on the distribution of impact velocities on Mars (Ivanov, 2001): (1) 1/2 of the escape velocity as an analogue to secondary cratering impact velocities $U_{sec} = \frac{U_{esc}}{2} \cdot sin(45) = 1.778\ km/s$ (2) escape velocity of $U_{esc} = 5.030\ km/s \cdot sin(45) = 3.556 km/s$ (3) average impact velocity $U_{avg} = 9.6\ km/s \cdot sin(45) = 6.8\ km/s$ (4) approximated maximum impact velocity $U_{max} = 22\ km/s \cdot sin(45) = 15.556\ km/s$. For each impact velocity and for both materials, 17 models with different impactor diameter L ranging from $0.1 - 100\ m$ were run. The impactor diameters were then recalculated using the same π_D, so that the crater diameter generated by such impacts should be approximately similar.

The relationship between the transient crater diameter and impactor diameter was used to derive a scaling law relationship. The dimensionless crater diameter ratio π_D (Equation 2.5) and the gravity-scaled size π_2 (Equation 2.7) were calculated for each models, for rock and sand, then plotted to find the scaling exponent β. By implementing these three values into Equation 2.13, the scaling coefficient K_D could be derived (Table 5.1 and Table 5.2 for sand).
The following model description setup is the same for all models, while the specific model setup for each of the rock and dust analogues are discussed in their own chapters below. In general, the model setup include two files: (1) An asteroid file with all parameters that describe the grid, resolution, global parameters, target parameters and so forth and (2) a material file that describes all models that are included to properly characterise the material and target. The target material consists of a single layer of basalt, and the impactor has the same composition as the material in each of the model setups. For the sand and basalt rock targets the ANEOS EoS for basalt (Pierazzo et al., 2005) is used. All general parameters that are used for both materials are presented in Table 3.1 below.
No viscoelasticity or acoustic fluidisation model was used as these are more relevant for complex crater modelling and we are interested in small simple craters. A thermal softening model is included in iSALE to approximate changes in shear strength due to temperature (Ohnaka, 1995). Also, a model to include weakening of materials with low density is included as a polynomial function of density, but will likely have no effects for small craters.

Table 3.1: General model parameters for both materials

Parameter	Symbol (unit)	Value
Equation of state	-	ANEOS Basalt
Gravitational acceleration	g (km/s^2)	3.711
Surface temperature	T (K)	218
Planet radius	r (km)	3390
Impactor velocity	U (km/s)	1.8, 3.6, 6.8, 15.6

3.2.1 Model setup basalt rock analogue

In addition to the models described above, three more models were included in the setup for the basalt rock analogue; a dilatancy model, rock strength model and a damage model. The basalt rock is assumed to have no initial porosity and as such no porosity model was included in this setup. A dilatancy model was included in iSALE by Collins (2014), and adds the effect of increased porosity due to shear deformation, which is most prominent during the modification stage of the impact process (Collins, 2014). Furthermore, a rock strength model was used to describe the yield strength Y of the material, and is defined as:

$$Y \; = \; Y_d \, D \; + \; Y_i(1 \; - \; D) \tag{3.1}$$

where D is a scalar measure computed by the damage model. In the model, the pre-impact surface is assumed to be intact. If the material is damaged, the equation for the yield strength becomes the same as for the damaged material strength, Y_d:

$$Y_d \; = \; min(Y_{d_0} \; + \; f_d \, p Y_{d_m}) \tag{3.2}$$

where Y_{d_0} is the cohesion of damaged material, f_d is the coefficient of internal friction for damaged material, p is pressure and Y_{d_m} is limiting strength at high pressures for damaged material. Finally, the intact material strength Y_i is defined as follows:

$$Y_i \; = Y_{i_0} \; + \; \frac{f_i \, p}{1 \; + \; \frac{f_i \, p}{Y i_m - Y i_0}} \tag{3.3}$$

where all the parameters are the same as for Equation 3.2 only for intact material, denoted by the subscript i. The values for the different parameters used in the model setup is from Collins (2014) and is summarised in Table 3.2.

Next, the COLLINS damage model for this setup calculates the damage D, which is used

in the yield strength equation (Eq. 3.1). It takes into consideration the shear failure (a function of plastic strain) and tensile failure. There are two model parameters for this damage model that has been used in this model setup, the brittle-ductile transition pressure and brittle-plastic transition pressure, where both are set to -1, which means that iSALE will choose these constants automatically.

Table 3.2: Model parameters for basalt rock.

Parameter	**Symbol (unit)**	**Value**
Poisson's ratio	-	0.25
Initial porosity	ϕ	Non-porous
Thermal parameters		
Melting temperature for basalt ($p = 0$)[1]	T_m (K)	1473
Specific heat capacity[2]	$(J/kg/K)$	850
Thermal softening parameter	ξ	1.2
Simon's approximation constant[2]	(Pa)	$4.5 \cdot 10^9$
Exponent in Simon's approximation[2]	-	3.0
Thermal gradient	(K/km)	0.01
Strength parameters (intact material)		
Cohesion of material[3]	Y_{i_0} (MPa)	10
Coefficient of internal friction[3]	f_i	2.0
Limiting strength at high pressure[1]	Y_{i_m} (GPa)	2.5
Strength parameters (damaged material)		
Cohesion of material[1]	Y_{d_0} (MPa)	0.01
Coefficient of internal friction[3]	f_d (-)	0.7
Limiting strength at high pressure	Y_{d_m} (GPa)	2.5
Damage parameters		
Brittle-ductile transition pressure	(Pa)	-1.0
Brittle-plastic transition pressure	(Pa)	-1.0
Dilatancy properties[3]		
Critical distension	α_c	1.2
Maximum dilatancy coefficient	β_{max}	0.045
Dilatancy pressure limit	p_{lim} (MPa)	200
Critical friction coefficient	f_c	0.4

[1] Watters et al. (2017)

[2] Pierazzo et al. (2005); Prieur et al. (2017)

[3] Collins (2014)

3.2.2 Model setup basalt sand analogue

The model setup for basalt sand analogue also includes the models that are stated in the introduction of this chapter. Two additional models are included, a strength model appropriate for granular material (Drucker-Prager) and a porosity model. In contrast to the setup for basalt rock, this setup does not include a damage model or dilatancy model.

The Drucker-Prager strength model (Drucker, 1951) defines the targets material yield strength Y as (note that this is similar to Equation 3.2):

$$Y \; = \; min(Y_0 \; + \; f\, p;\; Y_{LIM}) \tag{3.4}$$

where Y_0 is the cohesion which is the yield strength at $p = 0$, f is the coefficient of internal friction and Y_{LIM} is the limiting strength at high pressure (Prieur et al., 2017) (and iSALE manual). It is important to note that the coefficient of internal friction in the Drucker-Prager model f is defined differently than the Mohr-Coulomb coefficient of internal friction μ (Elbeshausen et al., 2009). Whereas μ (Mohr-Coulomb model) neglects the effect of the principal stress σ_2 ($\sigma_2 = \sigma_3$), f in the Drucker-Prager model is linked to all of the principal stresses σ_1, σ_2 and σ_3. Nevertheless, f and μ can be roughly related by $f \approx \mu\, cos\, \phi$ where ϕ is the angle of internal friction $\phi = tan^{-1}\mu$.

The presence of porosity in rocks can have a significant influence on the absorption of shock waves and temperature (Zel'dovich and Raizer, 1967; Collins et al., 2011). Therefore, a porosity model was used for the setup of the sand/dust models, called the $\varepsilon - \alpha$ compaction model (Wünnemann et al., 2006; Collins et al., 2011). This model describes the compaction and compression of pore space by the compaction function relating distension (collapse of the pores) α to volumetric strain ε_V. Distension is related to porosity, ϕ, by $\alpha = 1/(1 - \phi)$ in contrast to earlier models where the distension was computed from pressure (P-alpha model) (Wünnemann et al., 2006). The main governing equation used by iSALE computes the compaction of pores separately from the compression of the solid material (Herrmann, 1969) after the method of Carroll and Holt (1972):

$$P \; = \; f(\rho, E, \alpha) = \frac{1}{\alpha} P_s(\alpha, \rho, E) = \frac{1}{\alpha} P_s(\rho_s, E) \tag{3.5}$$

where P is the pore pressure, P_s is the pressure of the solid material, ρ and ρ_s is the pore and solid density respectively and E is the internal energy. Further, the model

describes the whole process of how intact pores become compacted and compressed and is divided into four regimes: (1) Elastic compaction - no changes in distension (2) Exponential compaction - rearranging of grains leading to decreased porosity (3) Power-law compaction - compaction becomes less rapid than in the previous regime, and (4) Compression - the porosity becomes zero. The distension is not directly calculated from the equations related to each regime, but rather from a compaction rate $\frac{d\alpha}{d\varepsilon}$ calculated for each regime (see Wünnemann et al. (2006) and Collins et al. (2011) for equations and more details regarding the regimes).

To use this model in iSALE five input parameters need to be chosen, α_0, α_χ ε_e, κ and χ. Where α_0 is the initial distension and α_χ is the distension in the transition between the exponential and power-law compaction regimes. ε_e is the elastic volumetric strain threshold where the compaction becomes irreversible. Furthermore, κ is the compaction rate parameter in the exponential compaction regime and χ is a ratio between the porous and solid material sound speed when the pressure is zero (Wünnemann et al., 2006; Collins et al., 2011; Prieur et al., 2017). In this thesis, the value for the parameters stated are from Prieur et al. (2017), where the parameters are chosen to be constant regardless of the initial porosity of the target material. The following values were employed: $\alpha_0 = 1.111$, $\varepsilon_e = 0$, $\alpha_\chi = 1.0$, $\kappa = 0.98$ and $\chi = 1$ for all of the basalt sand models. Table 3.3 sums up the model parameters used for sand.

Table 3.3: Model parameters for basalt sand.

Parameter	**Symbol (unit)**	**Value**
Poisson's ratio	-	0.25
Thermal parameters		
Melting temperature for basalt ($p = 0$)[1]	T_m (K)	1473
Specific heat capacity[2]	$(J/kg/K)$	850
Thermal softening parameter	ξ	1.2
Simon's approximation constant[2]	(Pa)	$4.5 \cdot 10^9$
Exponent in Simon's approximation[2]	-	3.0
Thermal gradient	(K/km)	0.01
Strength parameters (damaged material)		
Cohesion of material[1]	Y_{d_0} (MPa)	0.001
Coefficient of internal friction[3]	f_d	0.7
Limiting strength at high pressure	Y_{d_m} (GPa)	1.0
Porosity properties		
Initial porosity	ϕ_0	10%
Elastic threshold	ε_e	0.0
Transition (exponential to power-law)	α_χ	1.0
Exponential coefficient	κ	0.98
Sound speed ratio	χ	1.0

[1] Watters et al. (2017)

[2] Pierazzo et al. (2005); Prieur et al. (2017)

[3] Collins (2014)

3.2.3 Projectile material initial test

The initial test (Figure 3.2) was conducted to see whether the projectile material can influence the final crater diameter. This was done with model setup described in Table 3.2, one where the projectile had no internal strength (like water) and the other having the same material as the target.

The target with no internal strength does not need as much computational time as the impactor having the same material. Thus, it is interesting to see if the results were similar to each other. This was done to choose the model setup for the resolution test, in order to find a balance between good results and computational time. No significant differences between the two impactor materials were seen, and as such, the model with the fastest computational time was chosen, where the impactor had no internal strength.

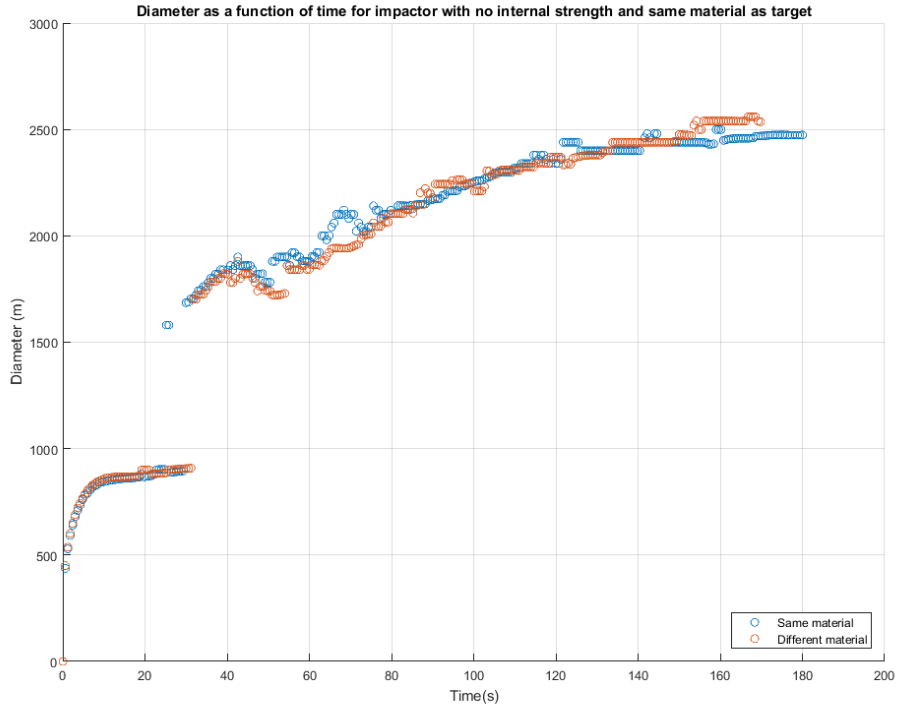

Figure 3.2: Shows the material test conducted for two impactor strengths: (1) no strength (e.g. different materials in red) and (2) impactor has the same strength as the target (Same material in blue))

3.2.4 Cells per projectile radius resolution test

A resolution test was performed to find a balance between satisfactory results and computational time. Several resolutions were tested (CPPR = 5, 10, 15, 20, 30) for both of the materials that are interesting in this thesis, basaltic rock-like material and basaltic dust, for a total of ten models. The resolution test was conducted for both of the materials to see if there were any difference between them regarding how much they were affected by the CPPR. For the ten models the asteroid diameter (L = 100m) and impact velocity (U = 6.8 km/s) were kept constant only varying the parameters that relate to the material. This means that for the five models with the same material, all parameters were constant except for the resolution so that the difference in transient crater diameter only could have been affected by the resolution. Table 3.2 and 3.3 above are the same parameters that were used in the resolution test.

The results from this test are shown in Figure 3.3 for the basaltic rock and Figure 3.4 for the basaltic sand. Both are normalised to the highest resolution tested (CPPR = 30). Prieur et al. (2017) found that no further increase of the CPPR over 10-15 will lead to higher accuracy in the estimation of the transient crater diameter. Due to time

as the most limiting factor, a CPPR = 10 was chosen for this project.

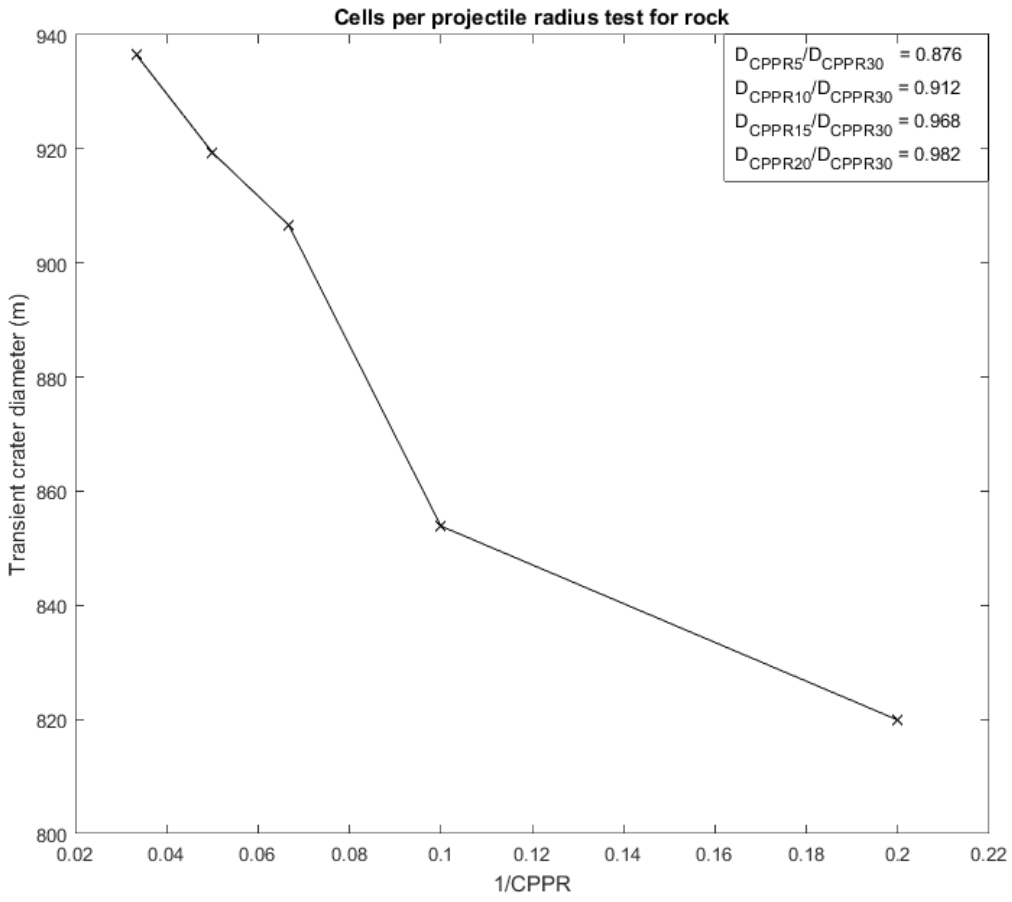

Figure 3.3: CPPR resolution test for rock normalised to CPPR = 30.

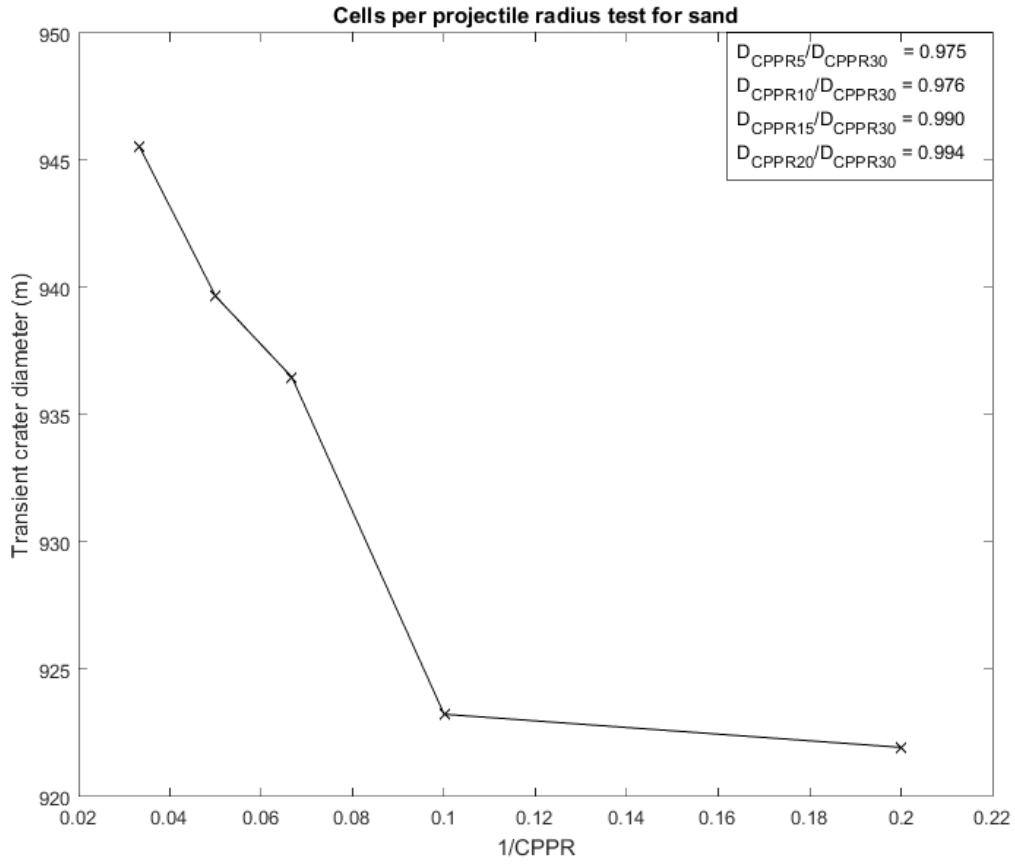

Figure 3.4: CPPR resolution test for sand normalised to CPPR = 30.

Chapter 4

Crater counting statistics at the InSight landing site

4.1 Basic principles of cratering statistics and extraterrestrial surface dating

The number of craters, binned by crater size, on a planetary surface can be used to estimate the age of the surface. To accurately derive ages, a good approximation of the impact flux throughout the Solar System is necessary. There are several models that suggest how the flux has changed: (1) a steady decay of the impact flux since at least the formation of the Moon (Neukum, 1983), (2) a spike in the flux at $\sim$ 3.9 Ga, Late Heavy Bombardment (Wetherill, 1975), (3) sawtooth decay (Morbidelli et al., 2012) and, (4) several spikes (Heavy Bombardment Eon) (Fritz et al., 2014).

On Earth, age determination of a geological unit is done directly by radiometric dating, but for most objects in the Solar System this is not possible. The Moon is the only other object from which such samples exist, and that the sampling site is known. To derive surface ages from other planetary objects, where no such samples exist, crater counting is the only tool available and is based on cratering statistics (Öpik, 1960; Werner and Ivanov, 2015). To derive a production size-frequency distribution (SFD), which is predicting the number of craters per unit surface area sorted by size (Ivanov, 2008), the following method is applied. First, mapping should be utilised to select an area that is geological homogeneous and thought to have the same age, followed by counting all of the craters in that specific area, summarised by the Crater Analysis Techniques Working Group (Arvison et al., 1979). If several areas of interest are counted, relative ages can be established. The main principle for deriving relative ages is that older areas will have accumulated more and larger craters than younger areas. However, in order

to derive an absolute model age, the SFD must be fitted to a crater-production function and a chronology model (Michael and Neukum, 2010; Werner and Ivanov, 2015). The crater-production function describes the SFD of craters on a planetary surface at a specific time (Ivanov, 2008; Werner and Ivanov, 2015). The surface must initially have zero craters and also not reached the saturation equilibrium, where newly formed craters will erase older craters (Ivanov, 2008). Two commonly used crater-production functions exist: (1) Hartmann production function (HPF) and, (2) Neukum production function (NPF) (reviewed in Neukum et al. (2001)). In this thesis, the saturation equilibrium curve used is from Hartmann (1984), production function from Ivanov (2001) and the chronology model from Hartmann and Neukum (2001).

Cratering chronology models describe how the impact rates in the Solar System have changed throughout time, for a specific reference crater diameter, and are calibrated from radiometric dating of lunar samples (Hartmann, 1981; Neukum and Ivanov, 1994; Neukum et al., 2001). For Mars, the cratering chronology model was transferred from the lunar cratering record, by considering the higher gravity of Mars and the change in the relative cratering rate (Neukum and Wise, 1976; Ivanov, 2001; Hartmann and Neukum, 2001; Neukum et al., 2001).

4.2 Crater counting

Crater counting was preformed for two areas near the InSight landing area in Elysium Planitia: (1) young lava flow (2) area covered with dust. These two areas were selected to test target properties, and this area of Elysium Planitia is quite young (Amazonian), thought to have more or less the same geological history, so that the material consist of only volcanic and dust deposits. Therefore, these two areas were deemed to be reasonable to use for crater counting.

The two areas were selected by using Thermal Emission Imaging System (THEMIS) infrared images from the 2001 Mars Odyssey orbiter (Christensen et al., 2003, 2004). The THEMIS data set features a spatial resolution of 100 m/pixel, and as such is used to identify surface materials and features, visible in these mid-resolution images. THEMIS measured the thermal inertia (resistance to change in temperature) of the surface. Areas with lower thermal inertia is displayed as dark areas in the data set, which is interpreted to represent fine particles such as dust and fine sand. In contrast, brighter areas have higher thermal inertia and are likely to be coarser particles or bedrock. Figure 4.1 features the rocky area, with the violet coloured outline representing the crater counting area and Figure 4.2 the sandy area with crater counting area in blue-green

colour.

For the crater counting, images from the High Resolution Imaging Science Experiment (HiRISE) on board the Mars Reconnaissance Orbiter were used, with a precise spatial resolution of 0.30 m per pixel (McEwen et al., 2007). An overview of the HiRISE images used and coordinates of the two areas is summed up in Table 4.1. In total, 4754 craters on a surface area of $41\,km^2$ were counted for the rock area. For the sand area 6533 craters were counted on a surface area of $6.4\,km^2$. The crater counting was done in ArcGIS (ESRI) using the CraterTools extension (Kneissl et al., 2011), which allows the combination and visualisation of multiple georeferenced datasets. To display and derive the SFD with isochrons, CraterStats 2 tool (Michael and Neukum, 2010; Michael et al., 2012) was used considering a minimum crater size of approximately 2 m.

Table 4.1: HiRISE images used and the coordinates for the crater counting areas.

HiRISE image	**Coordinates**
Rock area	
ESP_036550_1840	3.78°N 136.51°E
Sand area	
PSP_007118_1845	4.56°N 155.92°E

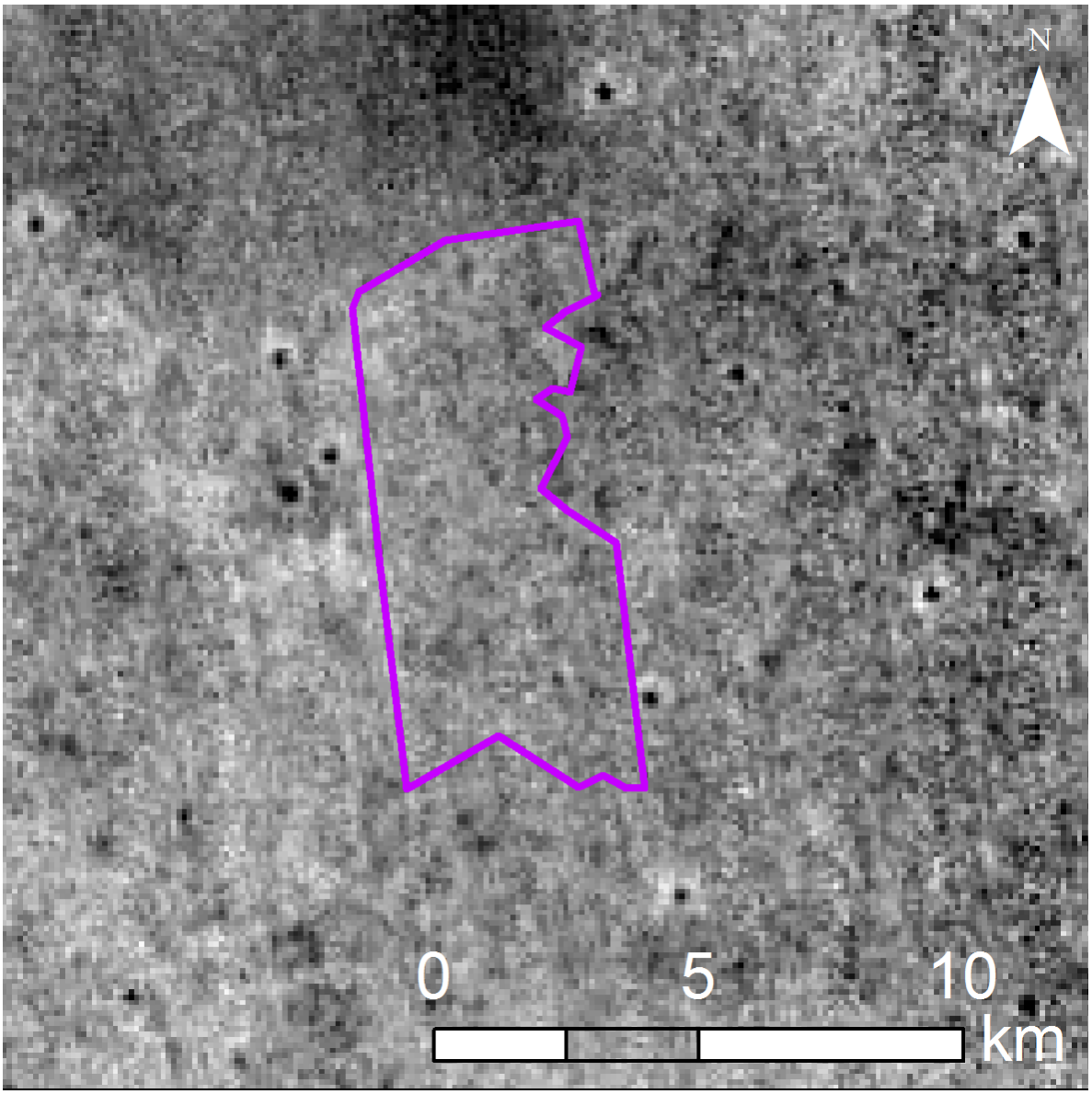

Figure 4.1: Mars THEMIS night mosaic 60N60S 100 m in Elysium Planitia. Area outlined in violet is the rock crater counting area (41 km^2).

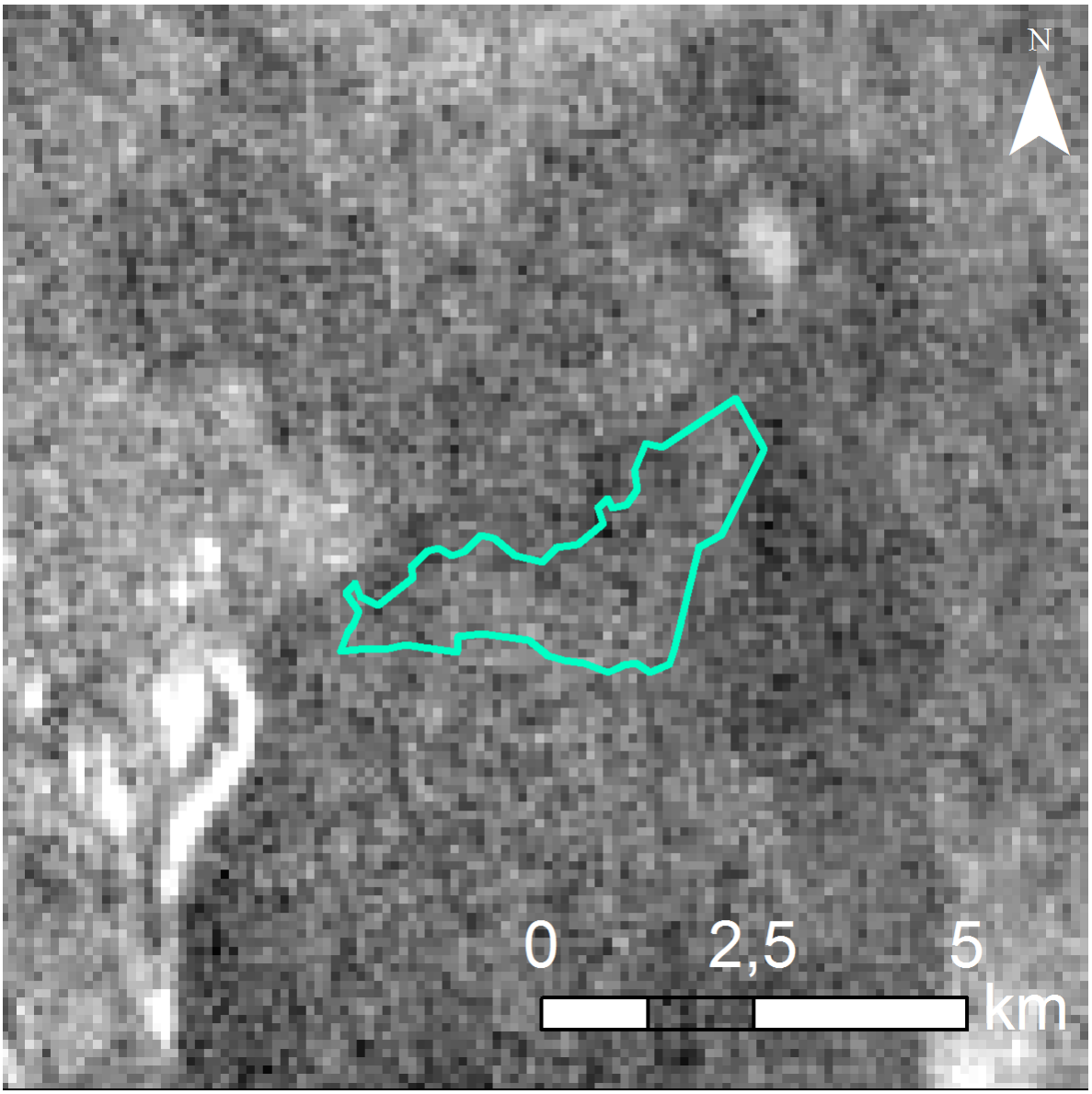

Figure 4.2: Mars THEMIS night mosaic 60N60S 100 m in Elysium Planitia. Area outlined in blue green is the sand crater counting area ($6.4\,km^2$).

Chapter 5

Results

The results from numerical modelling and crater counting are stated in this chapter. First, in Section 5.1 results from the numerical simulations are presented for rock and sand targets. Then in Section 5.2, the results from crater counting is presented followed by Section 5.3 where links between numerical modelling and crater counting were made.

5.1 Results from numerical modelling

The models were runned for four different impact velocities (maximum, average, escape and secondary) for a projectile range of 1 to 500 meters.

5.1.1 Cratering in rock targets

General observations for the evolution of the crater volume are that the volume increase dramatically at the start of the models. The crater volume then reaches a plateau, coinciding with the maximum crater volume (i.e. the transient crater) before the crater volume decreases. Also, the maximum volume was higher for larger projectile diameters than for smaller projectile diameters. In addition, the time it takes to reach the transient crater is longer for the largest impactor diameters compared to the smallest impactor diameters. This trend is also visible between the models with different impact velocity, when the impact velocity decreases; the transient crater time also decreases. For rock maximum velocity models (Figure 5.1) the transient crater was reached within approximately 50 s, and for average velocity (Figure 5.3) within 12 s. While for the escape (Figure 5.5) and secondary velocity (Figure 5.7) models, the transient crater was reached within 5 s and 2.5 s respectively.

For rock models with average, escape and secondary velocity abnormal behaviour at the end of the model run was observed (see Figure 5.3, Figure 5.5 and Figure 5.7) where

the volume started to increase again. For average velocity the increasing of volume started at about 90s, but earlier for escape ($\sim 30s$) and secondary ($\sim 6s$) velocity. It is also important to note that the models with the smallest impactor diameters ran for a shorter time than larger diameters. The run time for the secondary velocity models was also quite low at just 40 s for the longest running model. This might be due to the fact that for smaller impactors and velocity the computational time is longer, and therefore was not completely finished at the time when the models stopped.

A comparison of the transient and final crater diameter as a function of impactor diameter is viewed in Figure 5.2 (maximum velocity), Figure 5.4 (average velocity), Figure 5.6 (escape velocity) and Figure 5.8 (secondary velocity). The final crater diameter was computed at 4 times the transient crater time for models that had sufficient data. For models that did not finish, either 3 times the transient crater time was used, or were disregarded in total. The final crater diameters are larger than the transient crater, and the differences are largest in the secondary velocity model at $\sim 30\%$, and smallest in the maximum and average velocity models ($\sim 7 - 10\%$). In Figure 5.8 (secondary velocity) for comparison between the final and transient crater diameter it is apparent that the crater diameters do not follow a straight line, but changes quite vigorously (especially for the final crater) as the impactor diameter increases possibly due to the short run time or abnormal behaviour stated previously. This could perhaps be explained by the model setup and/or the included strength models. This issue is discussed further in Chapter 6. In Figure 5.9 π_D and π_2 values for the rock model are presented. These show that a higher velocity lead to higher π_D values. In Table 5.1 the derived scaling coefficient K_D and scaling exponent μ are summed up for the different velocities.

Table 5.1: Scaling relationships for the different rock velocities, written as $\pi_D = K_D \, \pi_2^{-\beta}$ where the scaling exponent β can be related to μ by $\mu = (2\beta)/(1-\beta)$.

U	K_D	β	μ
Maximum	2.4840	0.1905	0.47
Average	1.6443	0.2133	0.54
Escape	1.2603	0.2319	0.60
Secondary	3.2652	0.1220	0.28

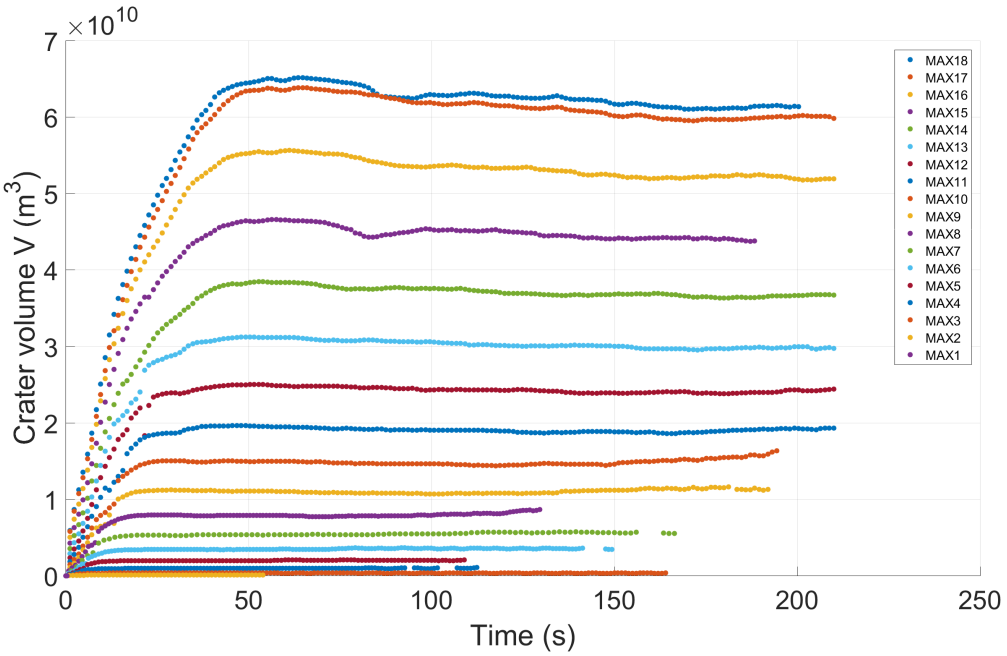

Figure 5.1: Volume as a function of time for rock target and maximum velocity.

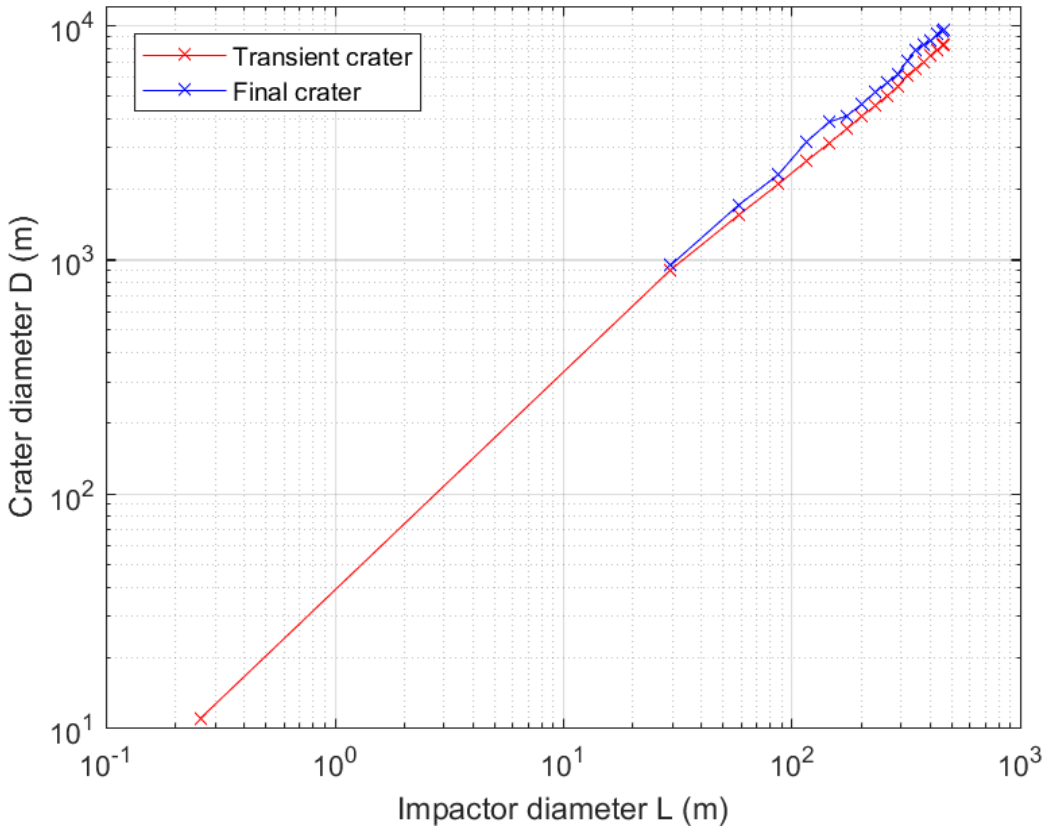

Figure 5.2: Transient and final crater diameter as a function of projectile diameter for rock target and maximum velocity.

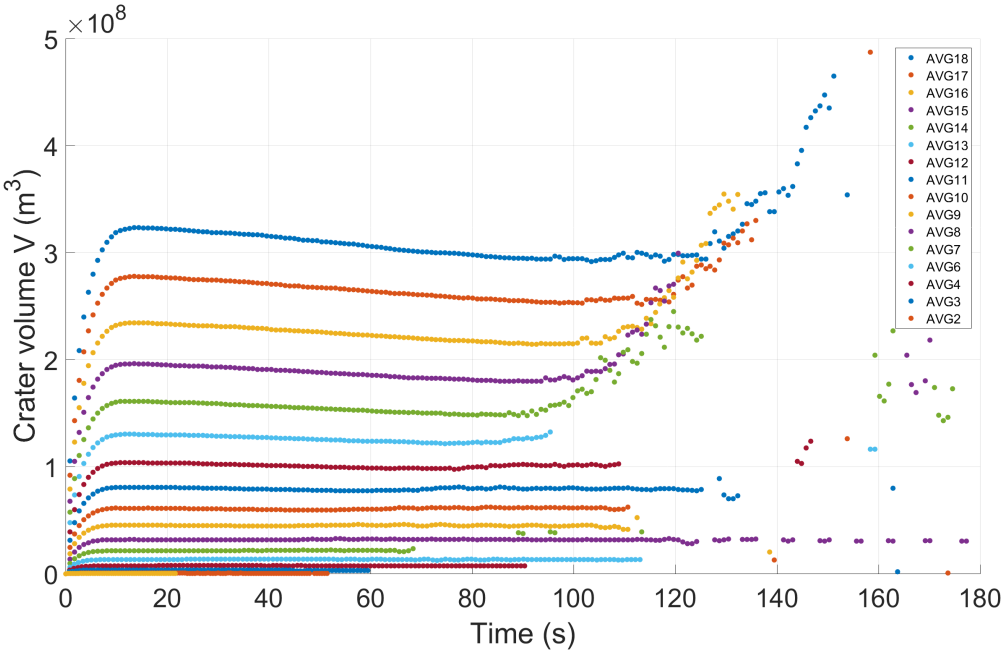

Figure 5.3: Volume as a function of time for rock target and average velocity.

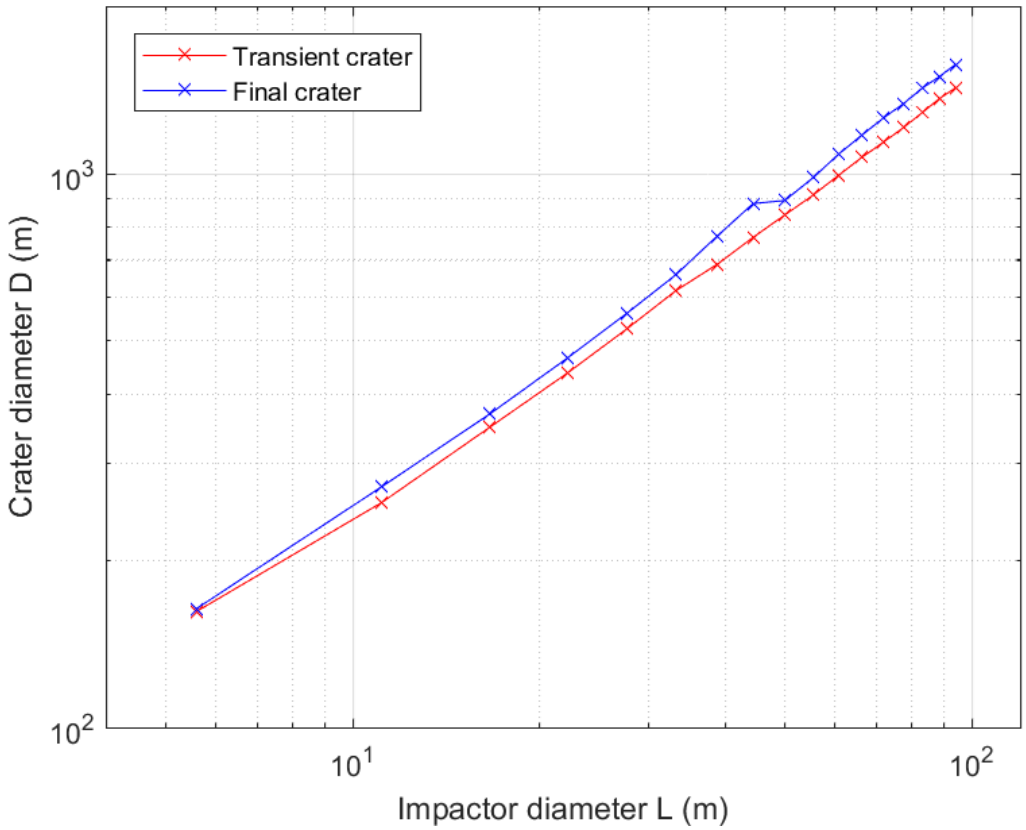

Figure 5.4: Transient and final crater diameter as a function of projectile diameter for rock target and average velocity.

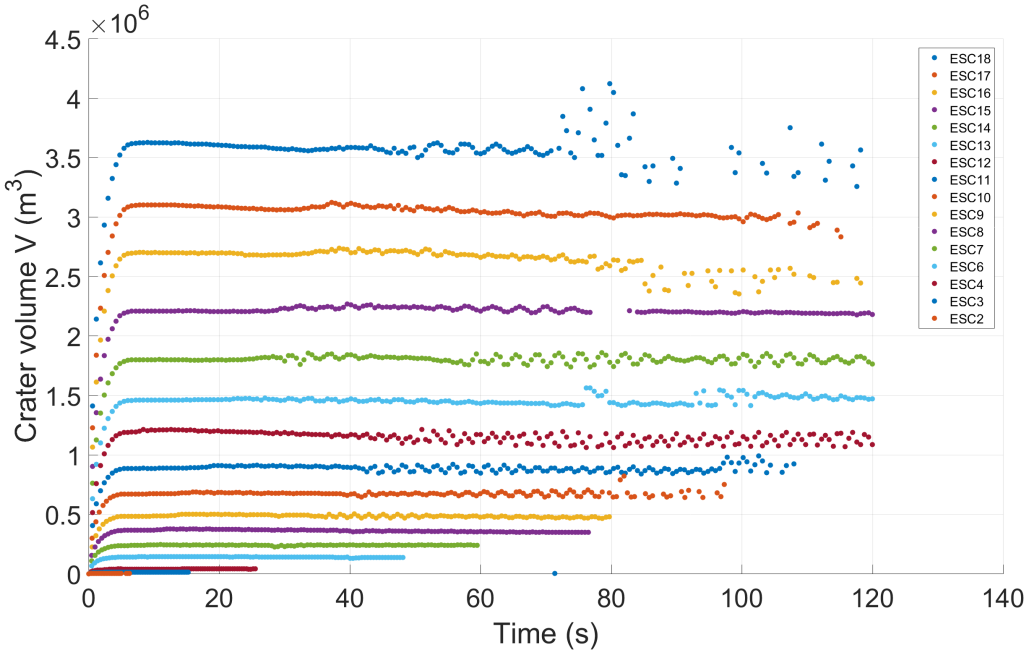

Figure 5.5: Volume as a function of time for rock target and escape velocity.

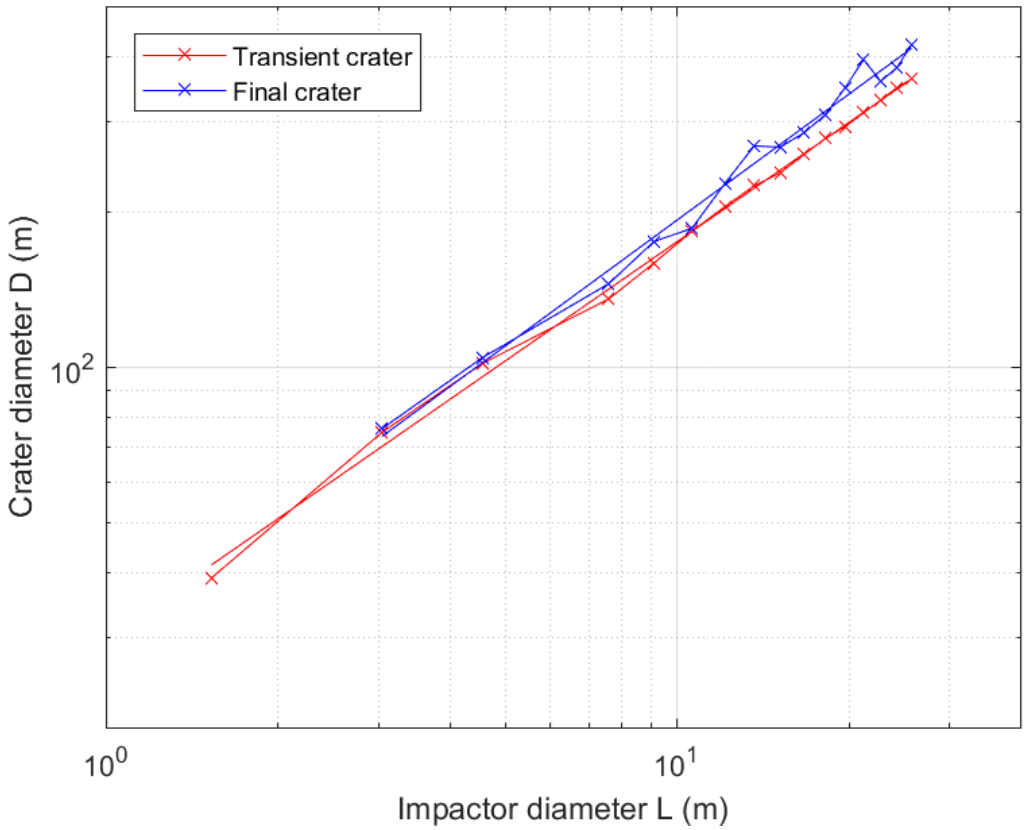

Figure 5.6: Transient and final crater diameter as a function of projectile diameter for rock target and escape velocity.

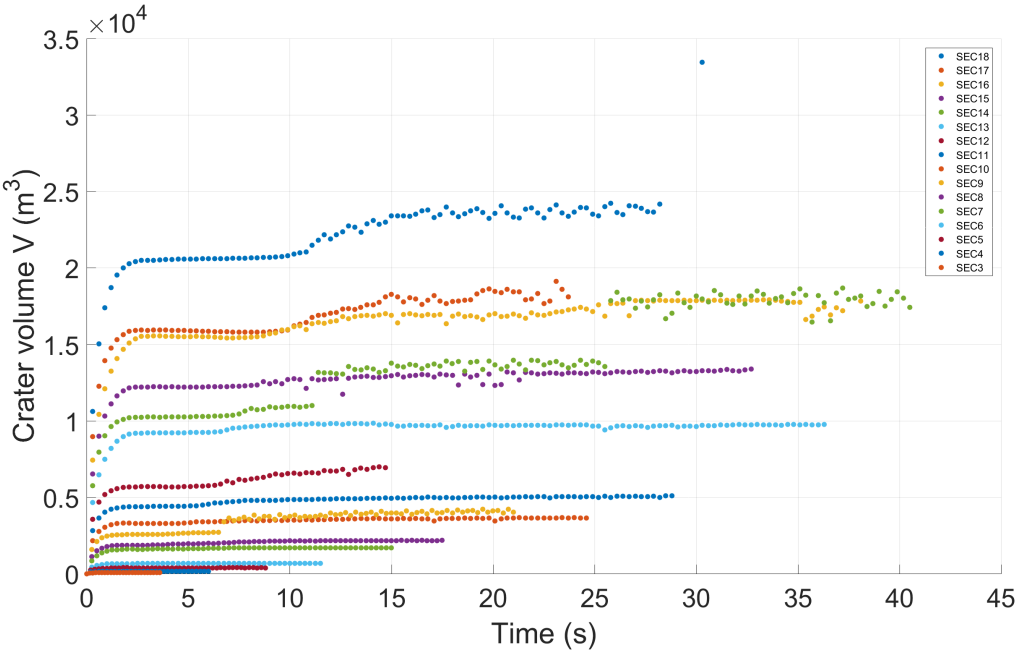

Figure 5.7: Volume as a function of time for rock target and secondaries velocity.

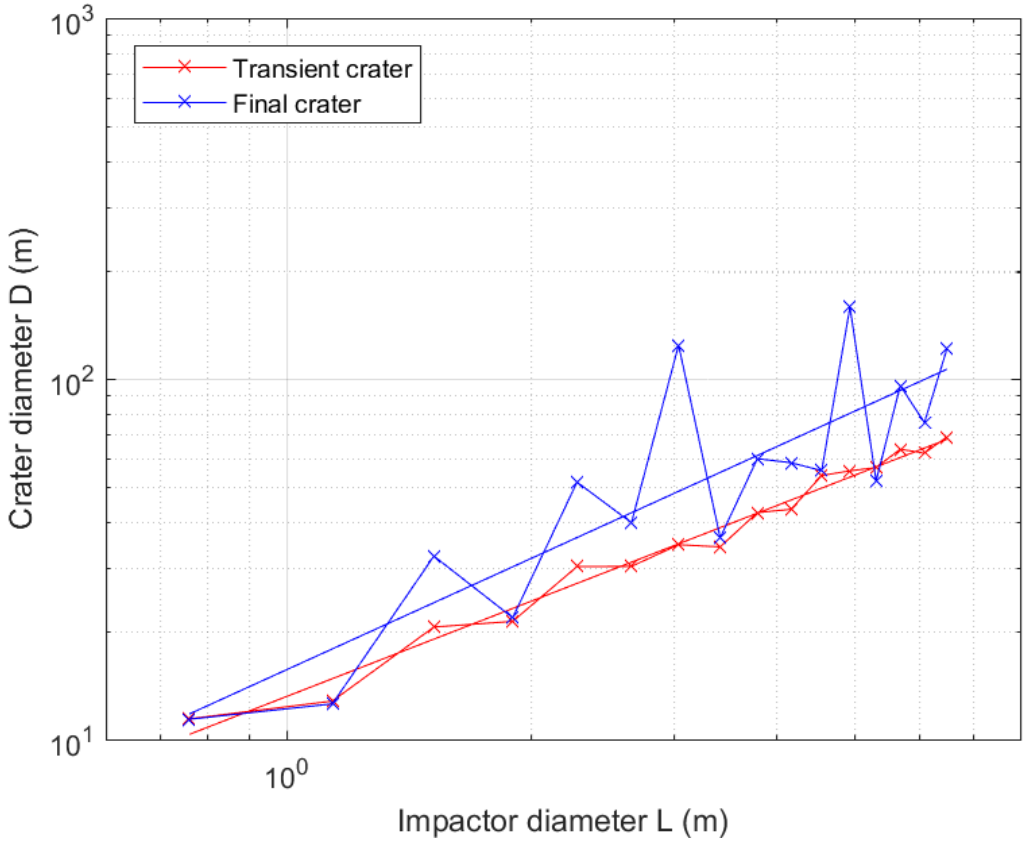

Figure 5.8: Transient and final crater diameter as a function of projectile diameter for rock target and secondaries velocity.

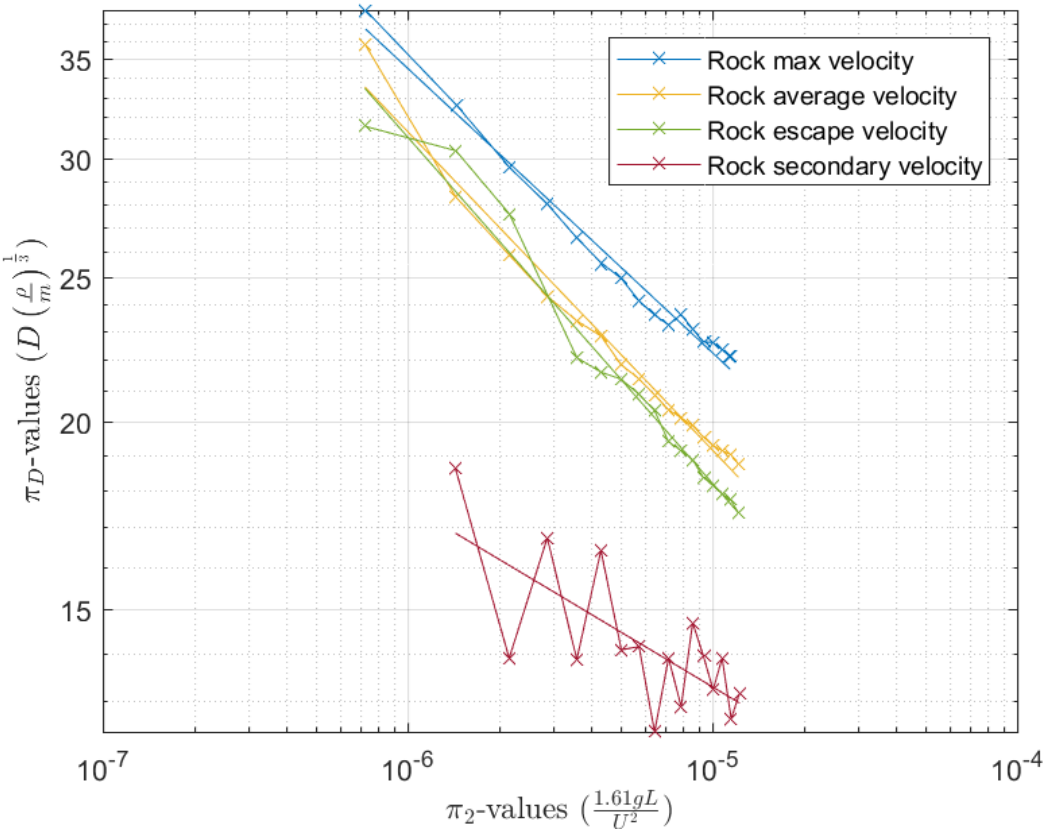

Figure 5.9: Dimensionless crater diameter (π_D) as a function of the gravity-scaled size (π_2) for rock target and all velocities.

5.1.2 Cratering in sand targets

As for the rock models, general observations for the sand model include: (1) rapid increase in the crater volume during the first part of the model runs, (2) crater volume reaches a maximum coinciding with the transient crater and then a steady decrease in the volume occur, (3) higher velocity increases the maximum volume observed (described for largest impactor diameter) , (4) the time it takes to reach the transient crater increases as the velocity increases, but also as the impactor diameter increase in each model, and lastly (5) run time for the larger impactor diameter was longer than for smaller impactor diameters (except for the maximum velocity model), especially visible in the model for secondary velocity. For the sand maximum velocity model (Figure 5.10) the transient crater is reached within $\sim 25s$ and for the average velocity model at $\sim 10s$ (Figure 5.12). The same goes for the escape velocity model (Figure 5.14) reaching the transient crater within the first $\sim 10s$. Additionally, the secondary velocity model (Figure 5.16) reaches the transient crater the fastest, within $\sim 3s$. In contrast to the rock models, no prominent increase in the crater volume after reaching the transient crater was observed.

Comparing the transient and final crater diameter as a function of impactor diameter; the maximum (Figure 5.11), average (Figure 5.13) and escape velocity (Figure 5.15) showed all a difference of $\sim 9\%$. The difference in the transient and final crater diameters seems consistent throughout the range of projectile diameters. As for the secondary velocity (Figure 5.17) an increase of the difference was observed ranging from almost no difference for the lowest comparable impactor diameter to about $\sim 15\%$ for the largest projectile diameter.
In Figure 5.18 π_D and π_2 values for the sand model are presented. As for the rock model, an increase in π_D was seen for models with higher velocity. In Table 5.2 the derived scaling coefficient K_D and scaling exponent μ for sand are summed up for the different velocities.

Table 5.2: Scaling relationships for the different sand velocities, written as $\pi_D = K_D\, \pi_2^{-\beta}$ where the scaling exponent β can be related to μ by $\mu = (2\beta)/(1-\beta)$.

U	K_D	β	μ
Maximum	4.1648	0.1469	0.34
Average	3.1350	0.1636	0.39
Escape	3.0199	0.1597	0.38
Secondary	2.8078	0.1581	0.38

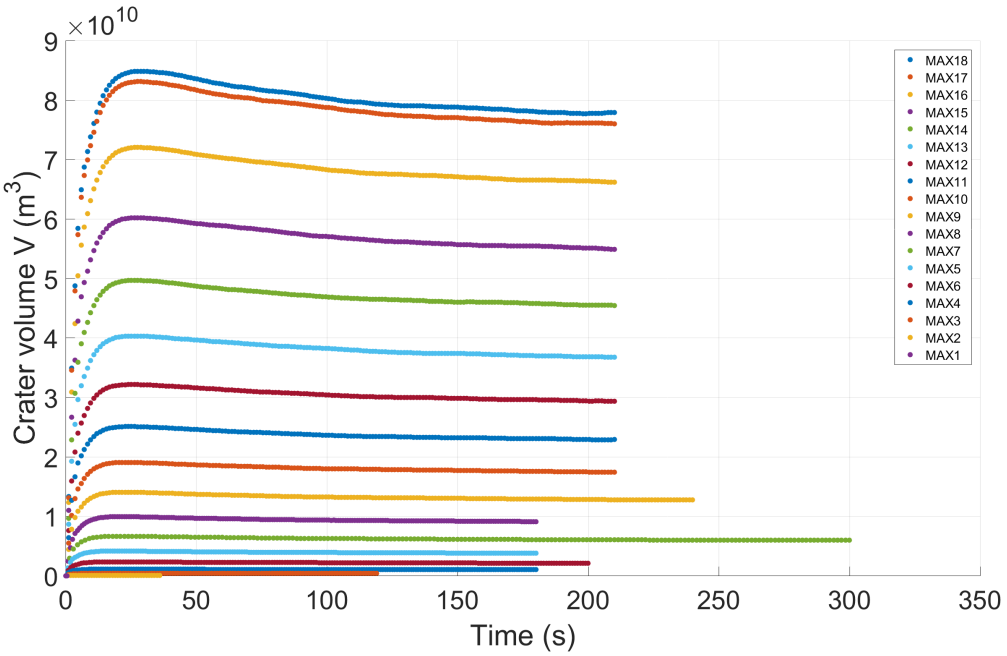

Figure 5.10: Volume as a function of time for sand target and average velocity.

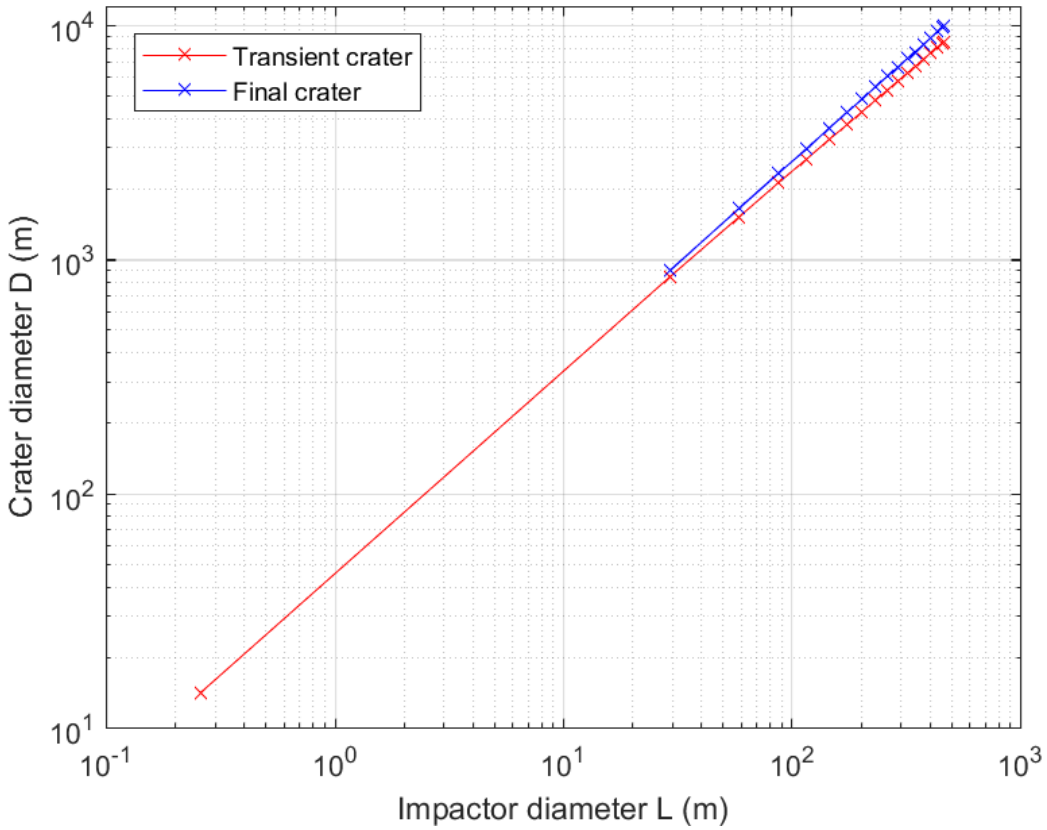

Figure 5.11: Transient and final crater diameter as a function of projectile diameter for sand target and maximum velocity.

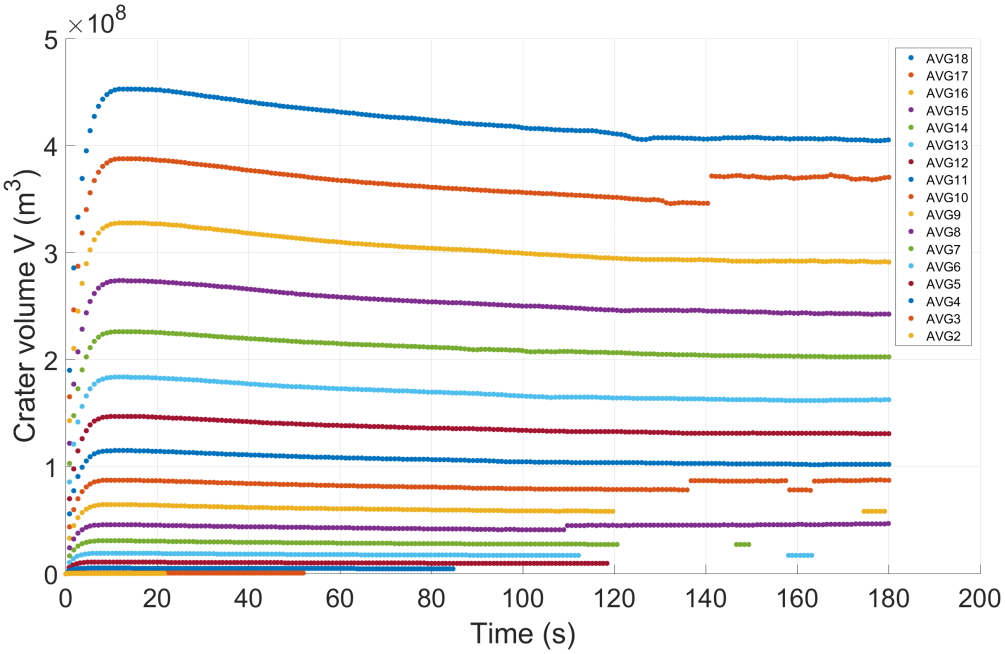

Figure 5.12: Volume as a function of time for sand target and average velocity.

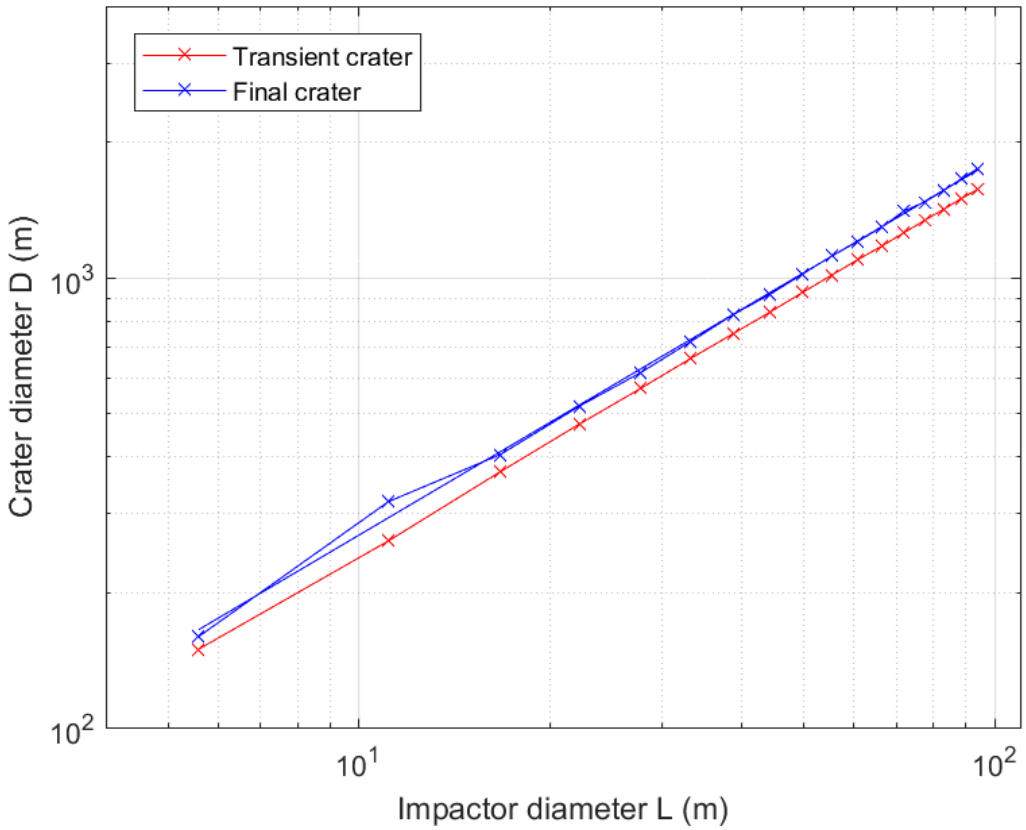

Figure 5.13: Transient and final crater diameter as a function of projectile diameter for sand target and average velocity.

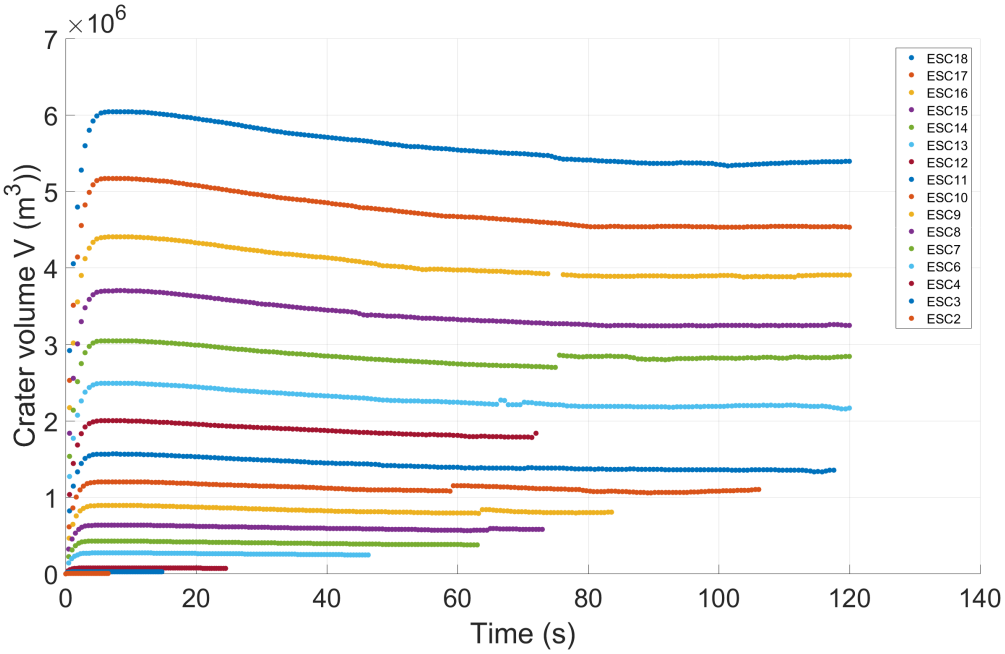

Figure 5.14: Volume as a function of time for sand target and escape velocity.

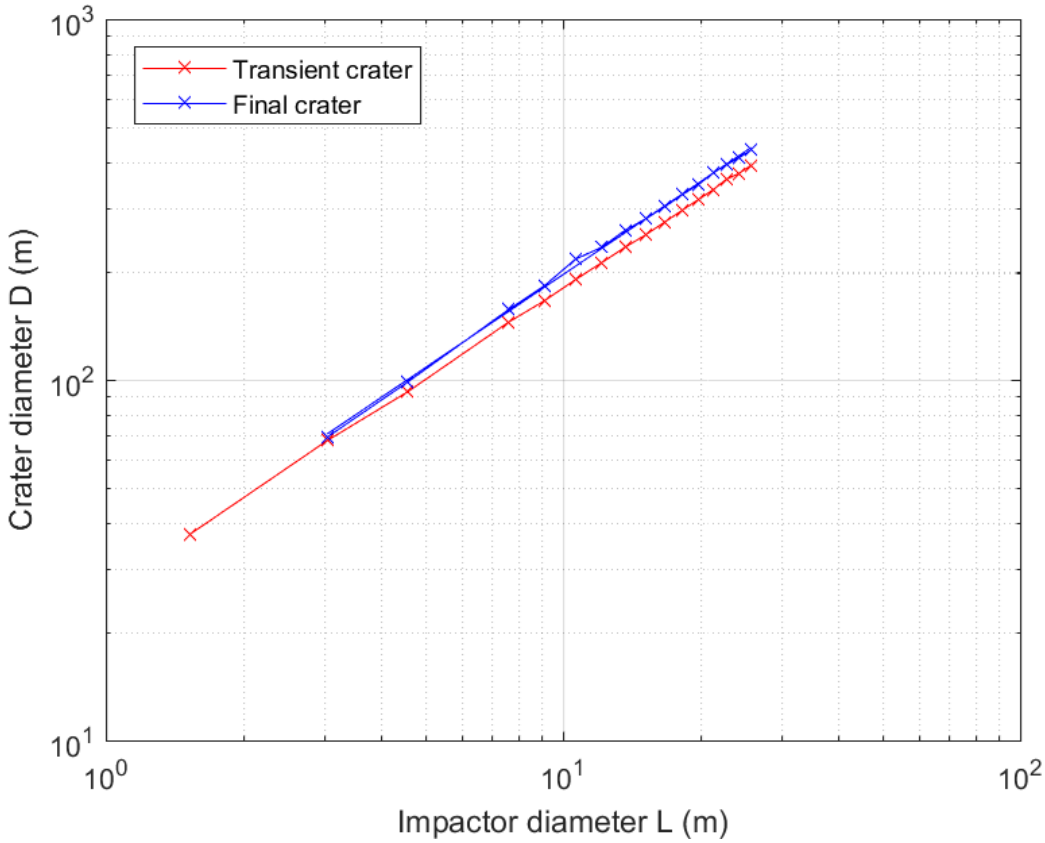

Figure 5.15: Transient and final crater diameter as a function of projectile diameter for sand target and escape velocity.

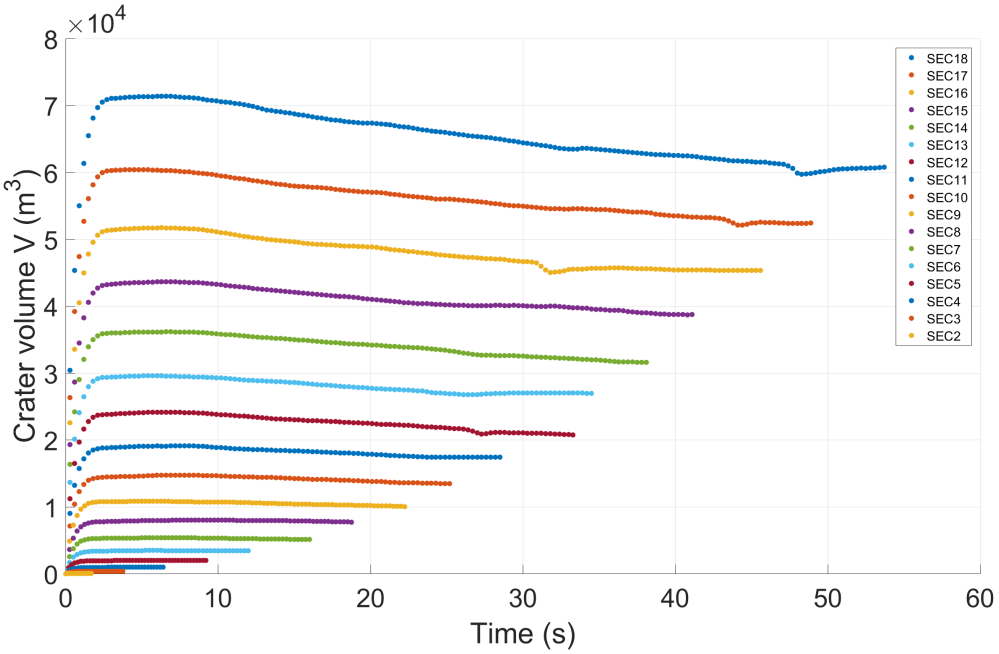

Figure 5.16: Volume as a function of time for sand target and secondaries velocity.

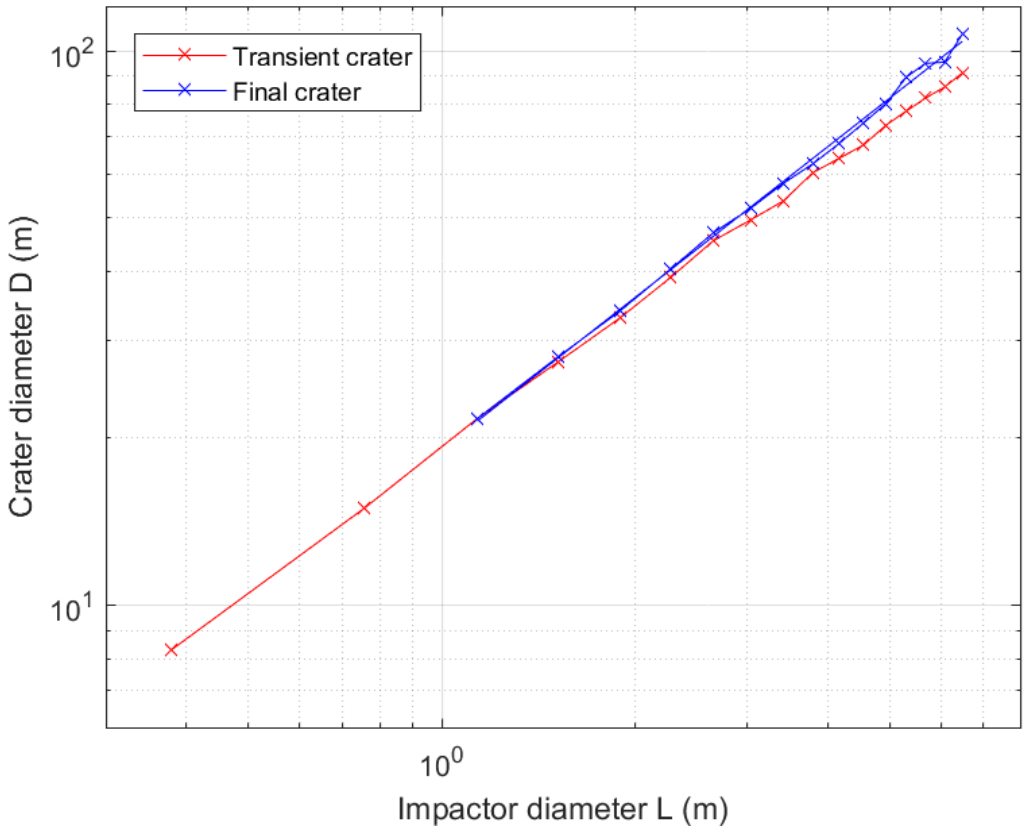

Figure 5.17: Transient and final crater diameter as a function of projectile diameter for sand target and secondaries velocity.

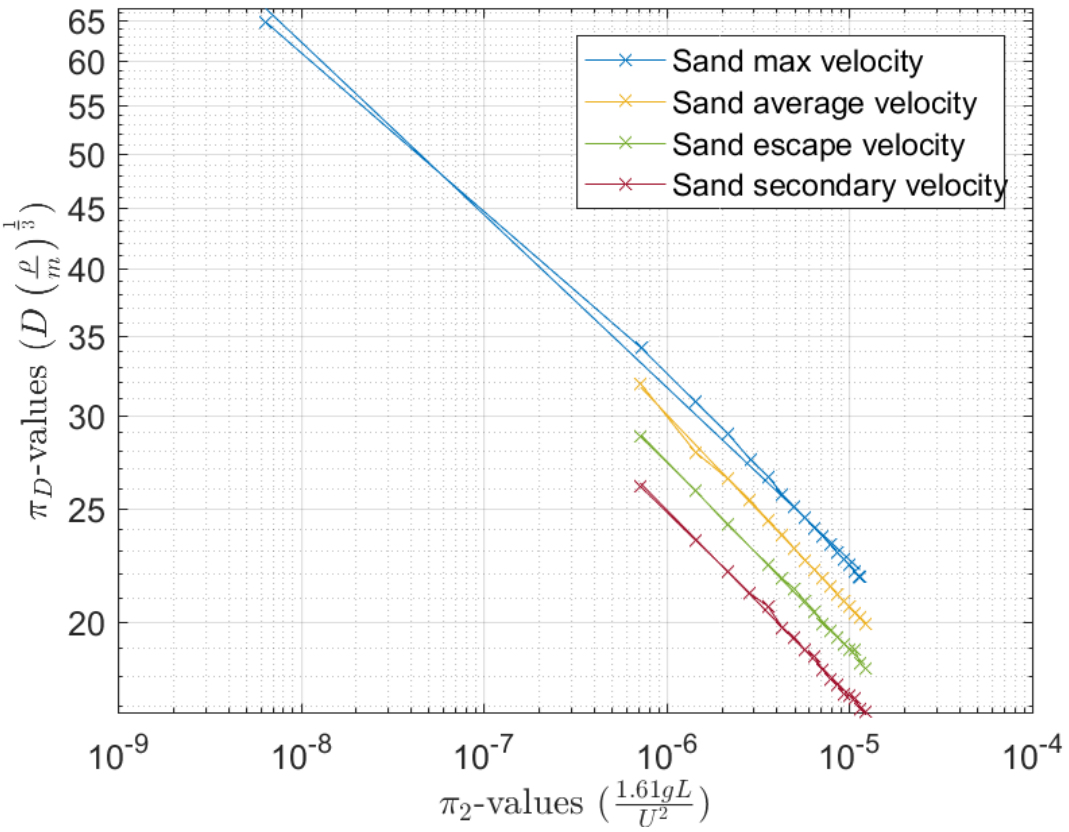

Figure 5.18: Dimensionless crater diameter (π_D) as a function of the gravity-scaled size (π_2) for sand target and all velocities.

5.1.3 Comparison between the rock and sand model

In Figure 5.19, final crater diameters as a function of impactor diameter is shown, for all velocities for both rock and sand targets. The first observation is that the size ranges changes as the velocity increases, higher impact velocity leads to larger final crater diameters. The final crater diameter range for secondary velocity is $\sim 10 - 100m$, escape velocity, $\sim 90 - 400m$. average velocity,$\sim 110 - 2000m$, and for maximum velocity, $\sim 1000 - 10000m$. From the plot of final crater diameter versus impactor diameter, the observation that impactor velocity influences the final crater diameter is shown. The four velocities share the same power-law, but show a marked increase in final crater diameter with increased velocity for the same impactor diameter. Both target properties do not seem to influence the power-law relationship, with the slopes for the same velocities being approximately equivalent.

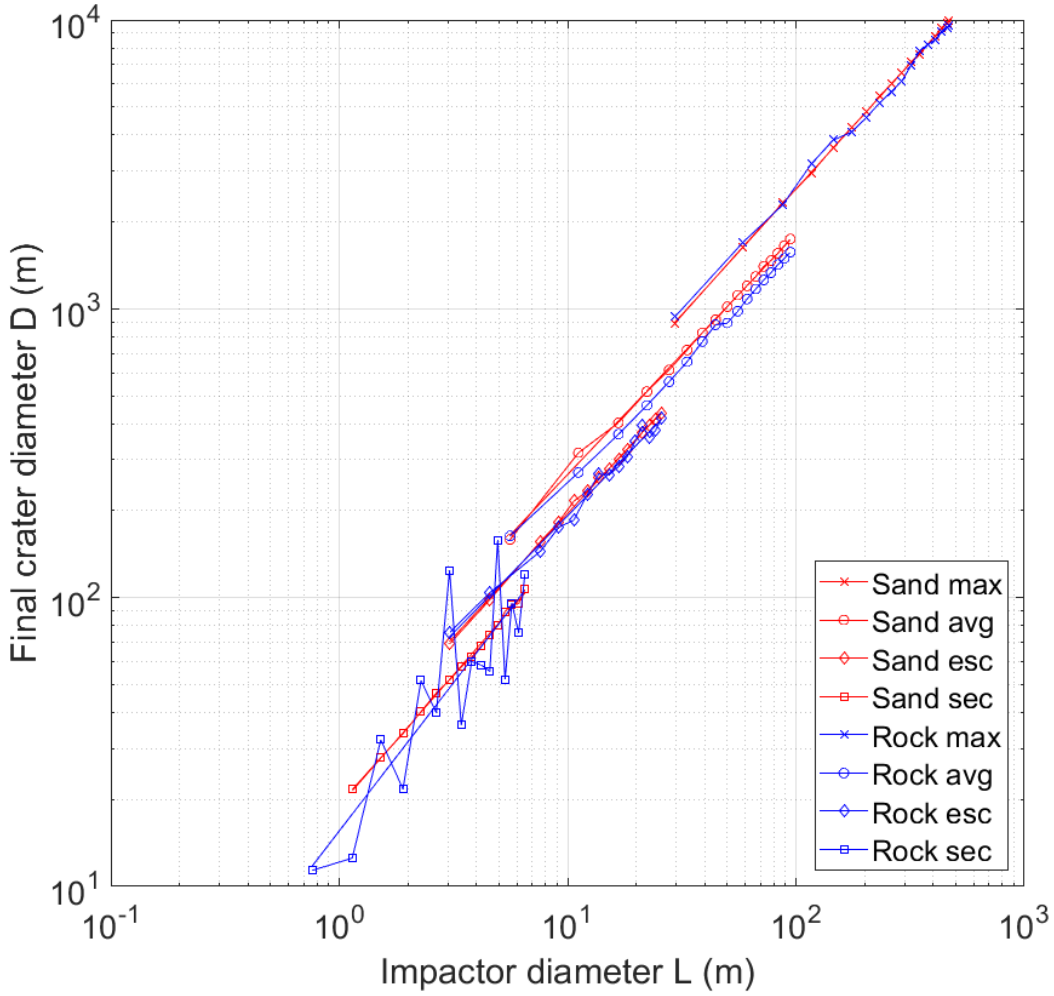

Figure 5.19: Final crater size comparison for rock and sand target for all velocities.

5.2 Results from crater counting

The units have been selected to resemble the target property difference in the numerical experiments. Figure 5.20 and Figure 5.21 show each of the entire counting unit (top) and a typical surface detail (bottom). In the sand equivalent crater counting area (Figure 5.21), the craters look more obscured compared to the rocky equivalent crater counting area (Figure 5.20). The sand area features what looks like dunes in some parts, and overall it looks like to some extent covered by dust. The thickness of the dust cover is not known, but does not feature major infill of the craters that are visible. The rocky area looks platy or rough compared to the sand area, and does not feature an extensive dust cover. At the boundary of the rock counting area in the northeast, what seems to be local dust is visible.

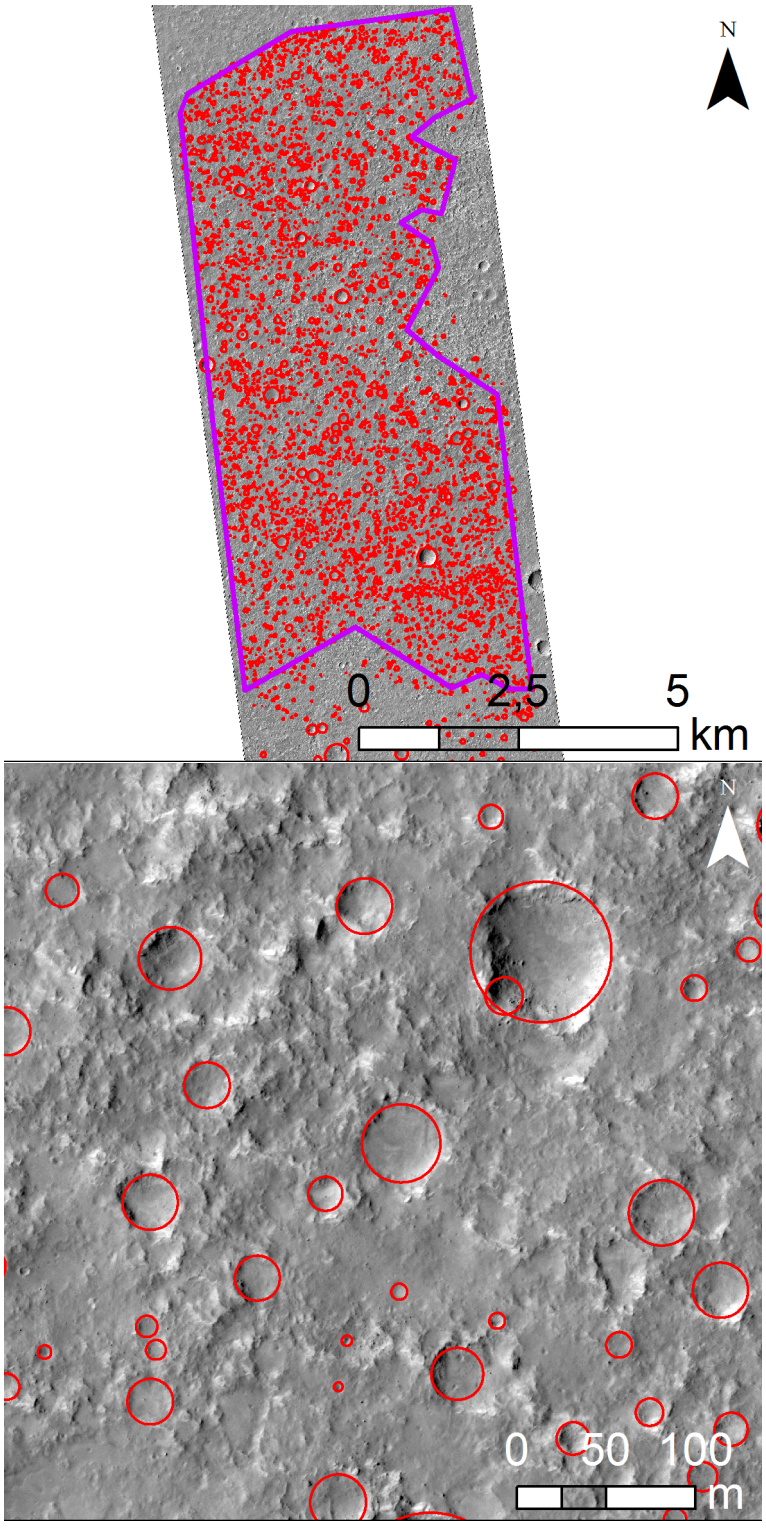

Figure 5.20: Overview of the crater counting area for rock (top) and typical surface detail (bottom).

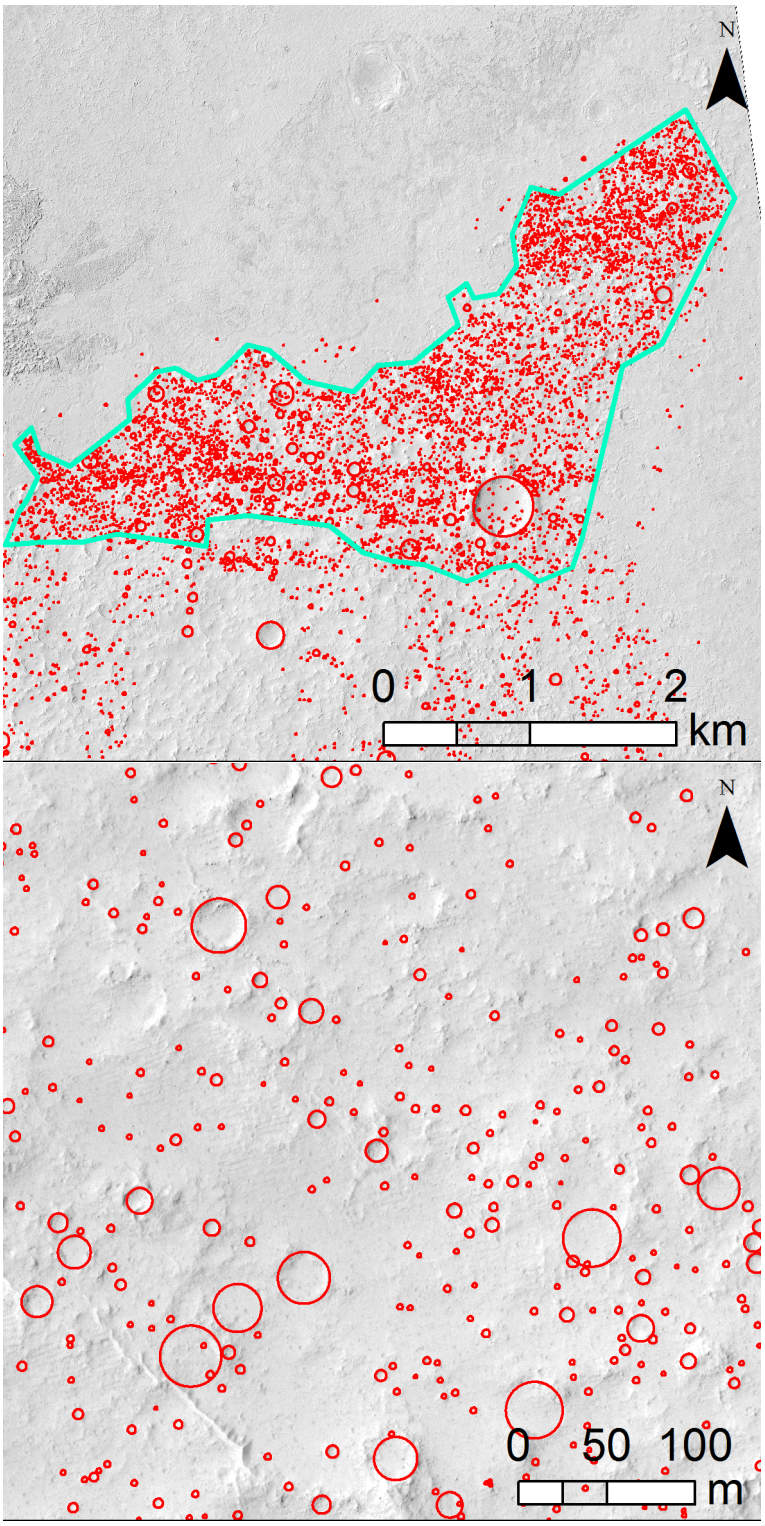

Figure 5.21: Overview of the crater counting area for sand (top) and typical surface detail (bottom).

Figure 5.22 shows the cumulative crater frequency as a function of crater diameter. The most prominent difference between the two counted areas, rock and sand, is the sandy area has more small craters than the rocky area. Starting by looking at the largest crater diameters from the bottom of the plot, the sand and rock follows approximately

the same slope until a crater diameter of 70 m where for smaller craters the curves start to deviate. The rocky area appear to have more large craters. For crater diameters of 70 m until 20 m the slope of the sand area gets shallower, while for the rock unit the slope is the same as craters 70 m until about 30 m and approximately following the 600 Ma isochron. At about 20 m crater diameter for both areas the slope decreases, most for the rock. For the sand unit, at 10 m, the slope gets steeper again and starting to level out at crater diameters less than 3 m. For rock unit, this change in slope starts at an earlier point and thus for a larger crater diameter, and reaches almost zero for craters below a couple of meters. The same is seen for the sandy area. Beyond the dashed line in Figure 5.22 the image resolution limits a concrete detection of crater (lower than 2 m). The other deviation from the isochron is considered to reflect one or two resurfacing events. While for the rock unit no further reliable age can be determined, for the resurfacing event for sand unit or could interpret two events for the range $\sim$ 70 - 20 meters and 10 - 2 meters.

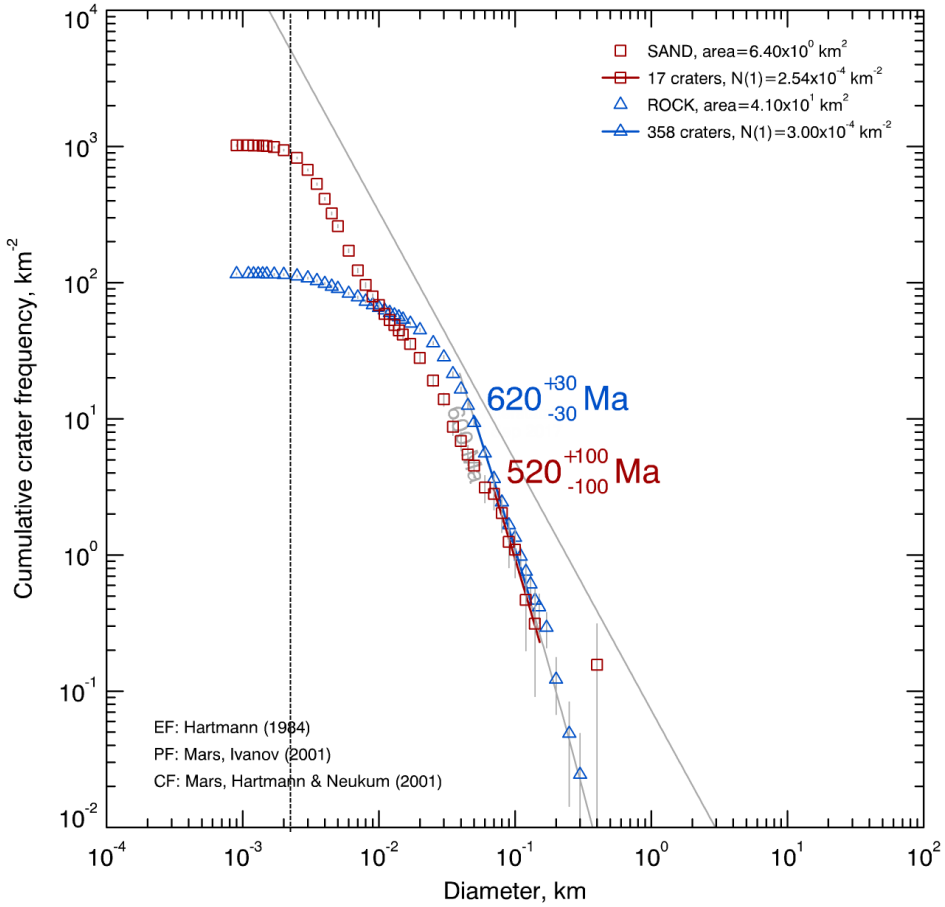

Figure 5.22: Cumulative crater frequency versus crater diameter for sand and rock area with isochron ages. For crater sizes below 2 m for sand area, the resolution limit detection of craters (denoted by the vertical dashed line). While the light grey sloped line is the equilibrium function, surfaces where craters are detected above this line is though to be saturated.

Because of the cumulative character of the crater SFD, it is a challenge to read directly the resurfacing timing. Therefore, one can apply a correction for the extraction of resurfacing events. Figure 5.23 for sand shows two resurfacing ages could be derived; at 540 Ma for a crater diameter range of 70 m to 170 m, and at 110 Ma for crater diameters between 25 m and 70 m. Although it may be possible to fit several resurfacing events for the rock unit, no corrections plots for the rock unit is provided here. The slope of the observed crater SFD is too shallow and no proper steepening back to the production function/isochron shape is observed. Such crater SFDs are then considered to show continuous resurfacing. For the comparison with the numerical experiments we first ignore that geological processes likely have modified the crater record and come back to this issue in the discussion.

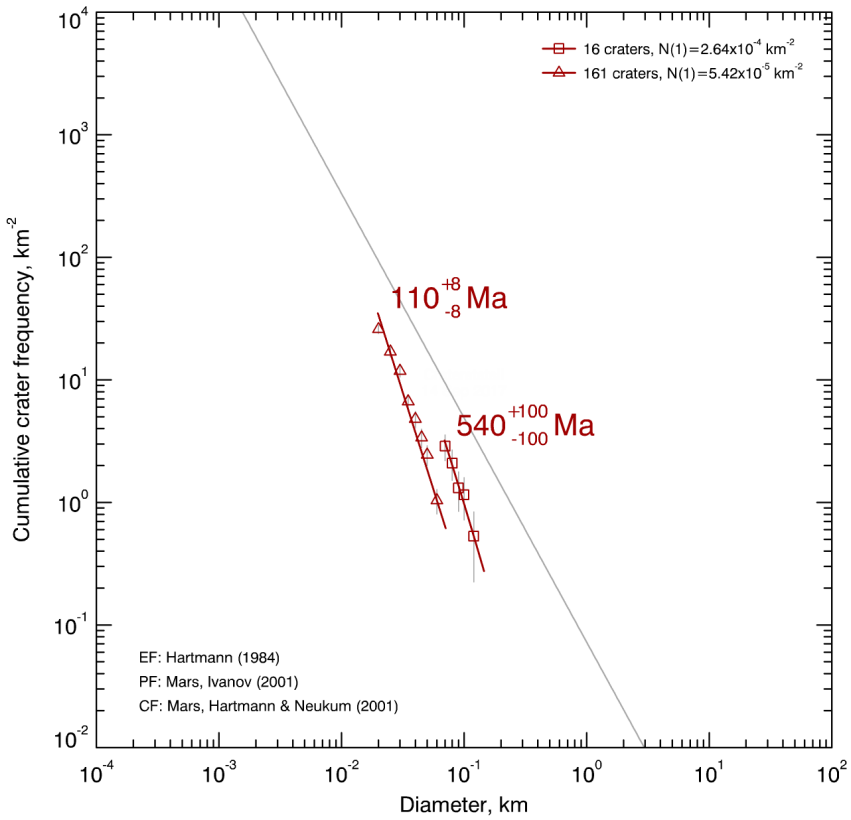

Figure 5.23: Cumulative crater frequency versus crater diameter corrected for for resurfacing for sand area with resurfacing ages. The light grey sloped line is the equilibrium function.

5.3 Coupling numerical modelling and crater counting

Figure 5.24 and Figure 5.25 feature a comparison of the derived cumulative SFD and power-laws derived from the numerical models. Several slopes was tested, but the two most relevant are presented here and the rest in Appendix A. Figure 5.24 compares the rock area crater count to power-laws derived from the rock models for all velocities; maximum, average, escape and secondary. To compare the numerical experiments and the observation it is assumes that the different slopes for the projectile distribution navigate from -2 to -4.

For crater diameters above 50 m the crater SFD follows the -2.5 slope for maximum velocity. As the crater SFD for rock levels out for crater diameters below 50 m, it was not possible to fit slopes for smaller crater diameters. Important to note that the same -2.5 power-laws are different for all the velocities. For example, for the slope of -2.5 for secondary velocity the slope is shallower. This also means that the craters produced by a smaller impact velocity still could have the same slope as for larger velocities. Also, larger crater diameters for sand (above 70 m) follows approximately the -2.5 slope for maximum velocity for rock. For Figure 5.25 for sand, crater diameters from 60 m to 100 m follows the -2 slope for maximum velocity. Additionally crater diameters between 20 m and 30 m lays in between the slopes for the maximum and average velocity slopes. Looking at smaller diameter range, 1 m to 10 m, this follows the -2 slope for sand escape velocity.

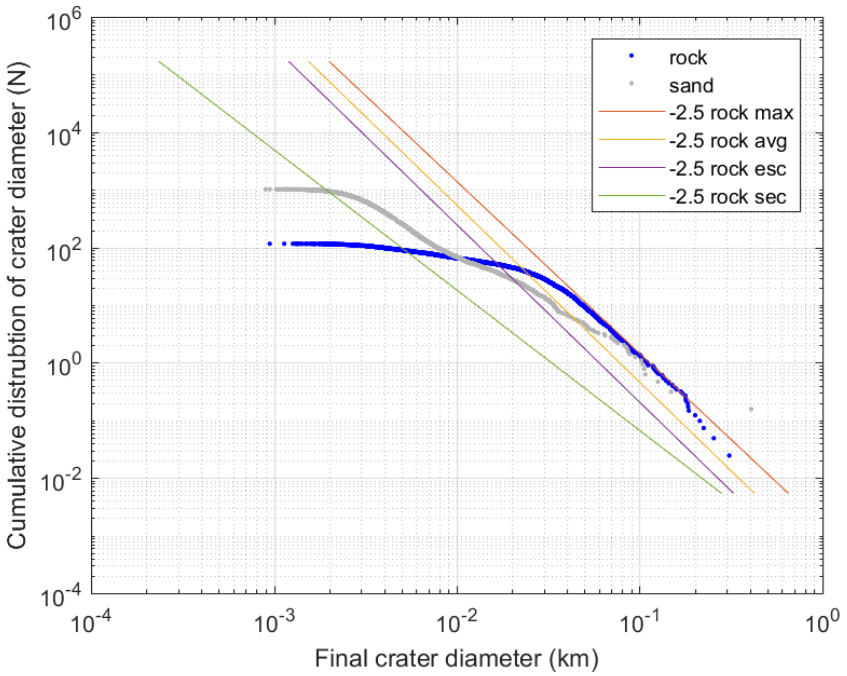

Figure 5.24: Cumulative distribution of crater diameter as a function of final crater diameter with -2.5 slopes for rock maximum, average, escape and secondaries velocity.

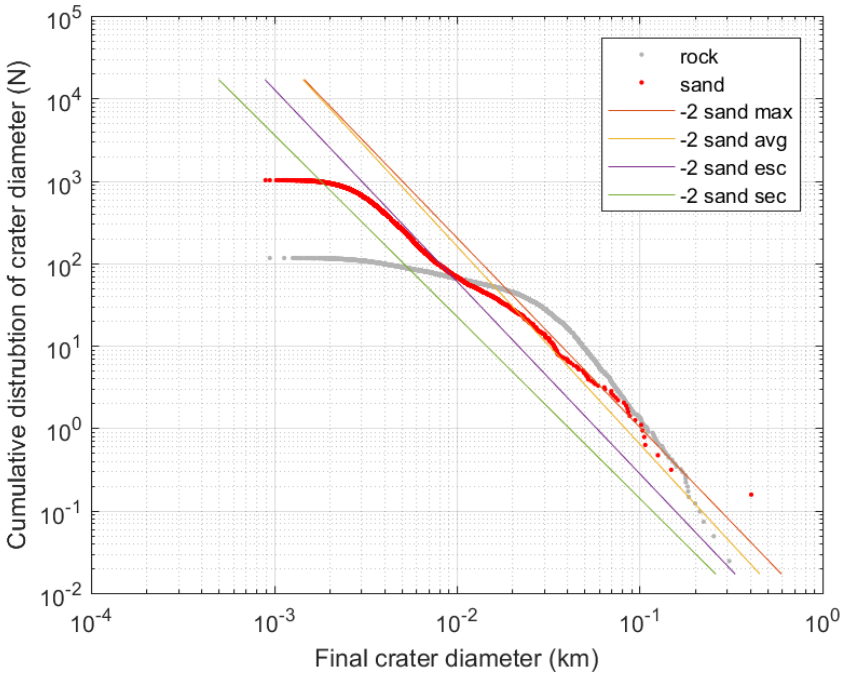

Figure 5.25: Cumulative distribution of crater diameter as a function of final crater diameter with -2.0 slopes for sand maximum, average, escape and secondaries velocity.

Chapter 6

Discussion

6.1 Numerical modelling discussion

In this work two main materials with different target properties were tested; basaltic rock and basaltic sand. Both of these models were a simplified analogue to the geology observed in Elysium Planitia, Mars. The main differences in the two models are the inclusion of different parameters to describe the behaviour of the target material. The rock model features dilatancy, rock strength and damage routines. For the sand target two models where included; a simplified strength model Drucker-Prager and a porosity model. So that the target properties investigated here are mainly the combination of cohesion and density of the target, including porosity. Thus, one can study the crater formation in different regimes.

In the sand models, the observed π scaling (Figure 5.18) follows the gravity scaling as expected for granular targets. Generally for both models, rock and sand, the effect of impact velocity is visible (Figure 5.9 and Figure 5.18) where a decrease in the impact velocity results in lower crater efficiency. From the maximum to secondary velocity, the decrease is about 24 % and 41 % for sand and rock models respectively. For simple impact craters formed in a cohesive materials such as rock, one expect that for smaller π_2 values the crater formation regime would fall into the strength regime, so that the π_D value becomes constant. This is not observed for the rock model in this work, and might be due to the incorporation of the dilatancy model. This might increase the porosity substantially, and thus reduce the coefficient of friction of the damaged target, so that the crater formation regime will only fall into the gravity regime. Numerical simulations done by Nowka et al. (2010) in non-porous target and a coefficient of friction of f=0.8, show that with a low cohesive strength (0 MPa and 0.1 MPa), π_2 and π_D follows a power-law that does not reach a constant π_D value, as might be the case for the rock models.

The behaviour of the rock models is different from what had been expected. In general, previous studies have shown scaling laws derived from targets with some cohesion possess both strength and gravity regimes. It is unclear why this is not the case. This behaviour seen in the rock models is also visible for two of the observed transient and final crater diameter versus impactor diameter plots for secondary velocity (Figure 5.8) where the points do not follow a straight line. This is visible in the π scaling plot (Figure 5.9) as well, especially for the lowest velocity. Holsapple and Housen (2017) stated that for small impact velocities $\sim 1km/s$ the point source approximation may no longer be valid, as well as the crater scaling laws for this case (Holsapple, 1993). In other words, the power-law for lower velocities might not follow a "normal" power-law function. This could be a possible explanation for the secondary rock case. Simple craters formed in the gravity regime will have a final crater diameter approximately 1.3 times the transient crater diameter (Werner and Ivanov, 2015). In this study, for the rock and sand models, the transient and final crater diameter ratios was lower than 1.3, except for the rock secondary velocity case (Figure 5.8) and to some extend also for the rock escape velocity case (Figure 5.6). In Figure 5.2, 5.4 and 5.6 the transient and final crater diameter for rock is about the same, while for secondary velocity the difference is notable (Figure 5.8).

The scaling coefficient and exponent are also affected by target properties as discussed by Prieur et al. (2017). Where it was found that the scaling coefficient was more dependent on the porosity of the target than the coefficient of friction while the opposite for the scaling exponent. For the rock models the K_D values ranged from 2.4840 (maximum velocity), 1.6443 (average velocity), 1.2603 (escape velocity) and 3.2652 (secondary velocity). The extremely high values for the maximum and secondary velocities are hard to explain, and it is uncertain to what may have caused these high values. For the secondary velocity, it might be because no scaling relation is reliable for such low velocity, but it is not clear. In comparison, the derived values for the average and escape velocity might be too low for the coefficient of friction (0.7) and 0 % porosity used in the model setup for rock. If the dilatancy model caused significant reduction in the target strength and thus increased porosity significantly this might explain the low K_D values observed.

For the sand model, the scaling coefficient were high; 4.1648 (maximum velocity), 3.1350 (average velocity), 3.0199 (escape velocity) and 2.8078 (secondary velocity). This is not expected for targets that are thought to be porous. Numerical experiments done by Prieur et al. (2017) and Wünnemann et al. (2011) show that the K_D values should decrease as the porosity decreases.

As for the scaling exponents for the rock models, the following values were derived: 0.47 (maximum velocity), 0.54 (average velocity), 0.60 (escape velocity) and 0.28 (secondary velocity). Again, the secondary velocity show abnormal behaviour, featuring a μ value that is less than the limits ($\mu = 1/3$ and $\mu = 2/3$). For the other velocities they lean towards energy scaling, and especially average and escape velocity coincide with values expected for non-porous targets derived from laboratory results ($\mu = 0.55 - 0.60$) (Holsapple and Schmidt, 1987). For the sand target μ values between 0.34 - 0.39 were derived, leaning closer to the momentum scaling that is coinciding with values for porous targets, typically in between 0.37 to 0.40 (Holsapple and Schmidt, 1987).

6.2 Crater counting discussion

Crater statistics were derived for two units in Elysium Planitia region thought to be equivalent to basaltic rock and basaltic sand/dust. The observed SFD in Figure 5.22 show a deviation from the production function at smaller diameters. The change in slope can be due to three factors: (1) target properties, (2) geological activity has erased, completely or partially, small craters, and (3) human error during the crater counting, and more than one factor could have played a role.

Several studies regarding SFD and the connection to target properties hinted that a difference that an inextricable mixture of material may alter the observed SFD (Dundas et al., 2010; Williams et al., 2014; Van der Bogert et al., 2017). Dundas et al. (2010) suggested that the age difference that was observed in Elysium Planitia and interpreted by Murray et al. (2005) as pack-ice, could instead be a result of target property variations across lava flows changing between platy and rigid type of lava, most apparent for crater diameters below 200 m. While, Williams et al. (2014) found that when accounting for elevation where the SFD where derived, the area had a younger age. Van der Bogert et al. (2017) found that the relative and absolute model age of impact melt was significantly lower than for the ejecta blanket, even though they must have formed at the same time.

The variations of target properties of an area with weaker properties than "rock" should be seen in the cumulative crater frequency plot as a steepening of the slope for the observed crater SFD function in comparison to the production function (Werner and Ivanov, 2015). Figure 5.24 and Figure 5.25 show that the slope for the rock area (-2.5) is slightly steeper than for the sand area (-2), for larger crater diameters (above 20 m).

This could be due to target properties, but the difference is minimal.

Geological activity might also be the reason for the change of slope in the crater SFD. Modifications of craters (erosion) and depositional effects, aeolian depositions and the emplacement of young lava flows, can alter an surface and obliterate smaller craters by infill of sediments or erosion (Werner, personal communication). Corrections for resurfacing was applied to see if it would alter the slope observed. The resulting SFD is shown in Figure 5.23 for sand area. The different ages might refer to possible resurfacing events, not the formation age, but no significant changes in the slope is seen. Note, that the correction could not be applied for any of the smallest craters or for the rock unit. Lastly, the differences could also be explained by the different structures for the two areas. While for the sandy area, small craters are easier to spot compared to the rougher rock area, and thus more small craters were counted in the sand area. Also note that the cumulative crater frequency looks discontinuous at 4 m, 10-20 m and 50 m for the sand area. This is possibly due to the lack of craters in those ranges in the areas, and/or crater diameter ranges that were possibly overlooked during the crater counting.

In general, geological activity or human error during crater counting seems the most plausible explanation based on the findings in this work. While there could be a difference in target properties visible at the surface, this dust layer might overlay harder basaltic lavas and thus not give expected behaviour. Also, the sand areas features what seem to be dunes, and infilling or erosion seems like the most reasonable explanation for the observed changes in slope the sand unit.

Crater counting relies heavily on manual counting of individual craters. With the availability of high-definition images, craters on the scale down to 1 m diameters can allow for more accurate age determination of planetary surfaces by identifying the most recent resurfacing events. The limitation to this technique, however, is that since the number of craters scale as a power law, increasingly the time is needed to manually count by several orders of magnitude. In the rock area, the rough texture of the surface made it difficult to distinguish craters at small diameters as several round-to-sub-round features could be interpreted as being textural differences, and not actually a crater. Therefore, human errors during crater counting could be a possible reason for the observed change in slope for craters smaller than 10 m for the rock unit. Due to the human limitation, it can be said that automation of some kind needs to be established to advance the crater counting technique. Recently attempts have been made to use machine learning to achieve this (e.g. DeLatte et al., 2018). The automation can be augmented by integration of optical images and Digital Elevation Models to distinguish

craters from non-craters using edge extraction methods, reducing complexity of the computation and leading to a significant reduction in false positives when compared with other methods (Yang and Kang, 2019). Although, this could be difficult for areas that feature major texture, such as observed in the rock unit, but could be a possible future implementation of in crater counting method.

6.3 Comparison

To explain the observed slopes of the measured SFDs, the impact projectile distribution in the rock scaling and in the sand scaling require different slope values. Because we cannot assume that the projectiles make a difference between unit target proprieties, one of the explanations then could be that the apparently similar observed slopes, and if the here derived scaling laws for rock and sand are correct, have a compensational effect. Also, because both in the rock and sand case the resulting slopes for scaling velocities are quite different than the other cases, one could suggest that for these young surfaces the number of secondary craters is small. While the coupling of both numerical modelling and crater SFD showed that the different slopes in one area could possibly be due to a change in velocity. However, one would not be able to explain why the projectiles hitting a geological unit at different speeds than the other.

Chapter 7

Conclusion

In this work, four different velocities for two different materials were tested in numerical experiments and crater counting for two equivalent target units was performed to see whether the modelled results could be observed for a real life case. Modelling of small craters are computationally intensive and may not acquire sufficient data for the smallest impactors. Careful planning for model setup and included regimes must be assured for accurate results. Results in this work show, that for low velocity impacts in rock target, this approach may not work and should be modelled with caution.
Other results, confirm the crater scaling laws, such as: (1) crater volume for higher velocities is larger than for lower velocity impacts for similar π_2 values and (2) velocity increases the π_D values observed for the same impactor diameters. The crater counting showed that the observed difference between the crater SFDs for rock and sand area could be be due to geological activity and/or target properties. In addition, the coupling of the numerical and cratering statistic results have shown that different slopes in the CSFD could be explained either by impacts with different impact velocities or/and by impacts in different types of units (most likely a combination of both). For example, a contamination of the CSFD by secondaries at small crater diameters (D $<$ 100 m) could explain the different slopes in the CSFDs (primary vs secondary impact velocities). In general, Mars feature a variety of materials often in the same geological unit, and as such the influence of target properties might be significant.

The work in this master thesis represent the first steps towards a better understanding the influence of impact velocity and target properties on CSFDs. Future work may include; (1) further exploration on how impact velocity changes the crater diameter, especially regarding simple craters in the strength regime, (2) improved model setup or regimes to accurately model small impact craters, (3) geological mapping of Mars to further understand how target properties vary with depth and across different geological units with complicated resurfacing history, and (4) numerical modelling of areas with permafrost to see how much ground ice affect final crater size.

Bibliography

Amsden, A., Ruppel, H., and Hirt, C. (1980). Sale: A simplified ale computer program for fluid flow at all speeds. Technical report, Los Alamos Scientific Lab., NM (USA).

Arvison, R., Boyce, J., and Chapman, C, a. o. (1979). Standard techniques for presentation and analysis of crater size-frequency data. *Icarus*, 37(2):467–474.

Beaty, D., Hays, L., Williford, K., and Farley, K. (2015). Sample science input to landing site selection for mars 2020: An in-situ exploration and sample caching rover. *Meteoritics and Planetary Science*, 50(S1):Art–No.

Buckingham, E. (1914). On physically similar systems; illustrations of the use of dimensional equations. *Physical review*, 4(4):345.

Carroll, M. and Holt, A. (1972). Static and dynamic pore-collapse relations for ductile porous materials. *Journal of Applied Physics*, 43(4):1626–1636.

Christensen, P. R., Bandfield, J. L., Bell III, J. F., Gorelick, N., Hamilton, V. E., Ivanov, A., Jakosky, B. M., Kieffer, H. H., Lane, M. D., Malin, M. C., et al. (2003). Morphology and composition of the surface of mars: Mars odyssey themis results. *Science*, 300(5628):2056–2061.

Christensen, P. R., Jakosky, B. M., Kieffer, H. H., Malin, M. C., McSween, H. Y., Nealson, K., Mehall, G. L., Silverman, S. H., Ferry, S., Caplinger, M., et al. (2004). The thermal emission imaging system (themis) for the mars 2001 odyssey mission. *Space Science Reviews*, 110(1-2):85–130.

Collins, G. (2014). Numerical simulations of impact crater formation with dilatancy. *Journal of Geophysical Research: Planets*, 119(12):2600–2619.

Collins, G. S., Melosh, H. J., and Ivanov, B. A. (2004). Modeling damage and deformation in impact simulations. *Meteoritics & Planetary Science*, 39(2):217–231.

Collins, G. S., Melosh, H. J., and Osinski, G. R. (2012). The impact-cratering process. *Elements*, 8(1):25–30.

Collins, G. S., Melosh, H. J., and Wünnemann, K. (2011). Improvements to the epsilon-alpha compaction model for simulating impacts into high-porosity solar system objects. *International Journal of Impact Engineering*, 38(6):434–439.

Collins, G. S., Wünnemann, K., Artemieva, N., and Pierazzo, E. (2013). Numerical modelling of impact processes. *Impact cratering: Processes and products*, pages 254–270.

DeLatte, D. M., Crites, S. T., Guttenberg, N., Tasker, E. J., and Yairi, T. (2018). Exploration of machine learning methods for crater counting on mars. In *Lunar and Planetary Science Conference*, volume 49.

Dence, M., Grieve, R. A., and Robertson, P. (1977). Terrestrial impact structures-principal characteristics and energy considerations. In *Impact and explosion cratering: Planetary and terrestrial implications*, pages 247–275.

Dienes, J. and Walsh, J. (1970). Theory of impact: Some general principles and the method of eulerian codes. In *High-velocity impact phenomena*, volume 2, pages 25–104. Academic Press New York.

Drucker, D. C. (1951). A more fundamental approach to plastic stress-strain relations. In *Proc. of 1st US National Congress of Applied Mechanics, 1951*, pages 487–491.

Dundas, C. M., Keszthelyi, L. P., Bray, V. J., and McEwen, A. S. (2010). Role of material properties in the cratering record of young platy-ridged lava on mars. *Geophysical Research Letters*, 37(12).

Elbeshausen, D., Wünnemann, K., and Collins, G. S. (2009). Scaling of oblique impacts in frictional targets: Implications for crater size and formation mechanisms. *Icarus*, 204(2):716–731.

Farley, K., Malespin, C., Mahaffy, P., Grotzinger, J., Vasconcelos, P., Milliken, R., Malin, M., Edgett, K., Pavlov, A., Hurowitz, J., et al. (2014). In situ radiometric and exposure age dating of the martian surface. *science*, 343(6169):1247166.

Fritz, J., Bitsch, B., Kührt, E., Morbidelli, A., Tornow, C., Wünnemann, K., Fernandes, V. A., Grenfell, J., Rauer, H., Wagner, R., et al. (2014). Earth-like habitats in planetary systems. *Planetary and Space Science*, 98:254–267.

Gault, D. E., Quaide, W. L., and Oberbeck, V. R. (1968). Impact cratering mechanics and structures. In French, B. M. and Short, N. M., editors, *Shock Metamorphism in Natural Materials*, pages 87–99. Mono Book Corp., Baltimore.

Gault, D. E. and Wedekind, J. A. (1978). Experimental studies of oblique impact. In *Lunar and Planetary Science Conference Proceedings*, volume 9, pages 3843–3875.

Golombek, M., Kipp, D., Warner, N., Daubar, I. J., Fergason, R., Kirk, R. L., Beyer, R., Huertas, A., Piqueux, S., Putzig, N., et al. (2017). Selection of the insight landing site. *Space Science Reviews*, 211(1-4):5–95.

Hartmann, W. K. (1981). Chronology of planetary volcanism by comparative studies of planetary cratering. *Basaltic Volcanism on the Terrestrial Planets.*, pages 1049–1127.

Hartmann, W. K. (1984). Does crater "saturation equilibrium" occur in the solar system? *Icarus*, 60(1):56–74.

Hartmann, W. K. and Neukum, G. (2001). Cratering chronology and the evolution of mars. In *Chronology and evolution of Mars*, pages 165–194. Springer.

Herrmann, W. (1969). Constitutive equation for the dynamic compaction of ductile porous materials. *Journal of Applied Physics*, 40(6):2490–2499.

Holsapple, K. (1993). The scaling of impact processes in planetary sciences. *Annual review of earth and planetary sciences*, 21(1):333–373.

Holsapple, K. and Schmidt, R. (1987). Point source solutions and coupling parameters in cratering mechanics. *Journal of Geophysical Research: Solid Earth*, 92(B7):6350–6376.

Holsapple, K. A. and Housen, K. R. (2007). A crater and its ejecta: An interpretation of deep impact. *Icarus*, 191(2):586–597.

Holsapple, K. A. and Housen, K. R. (2017). Craters from impacts and explosion.

Ivanov, B. (2008). Size-frequency distribution of asteroids and impact craters: Estimates of impact rate. In *Catastrophic events caused by cosmic objects*, pages 91–116. Springer.

Ivanov, B., Deniem, D., and Neukum, G. (1997). Implementation of dynamic strength models into 2d hydrocodes: Applications for atmospheric breakup and impact cratering. *International Journal of Impact Engineering*, 20(1-5):411–430.

Ivanov, B. A. (2001). Mars/moon cratering rate ratio estimates. *Space Science Reviews*, 96(1-4):87–104.

Kenkmann, T., Collins, G. S., and Wünnemann, K. (2012). The modification stage of crater formation. *Impact cratering: Processes and products*, pages 60–75.

Kneissl, T., van Gasselt, S., and Neukum, G. (2011). Map-projection-independent crater size-frequency determination in gis environments—new software tool for arcgis. *Planetary and Space Science*, 59(11-12):1243–1254.

Kurosawa, K. and Takada, S. (2019). Impact cratering mechanics: A forward approach to predicting ejecta velocity distribution and transient crater radii. *Icarus*, 317:135–147.

McEwen, A. S., Eliason, E. M., Bergstrom, J. W., Bridges, N. T., Hansen, C. J., Delamere, W. A., Grant, J. A., Gulick, V. C., Herkenhoff, K. E., Keszthelyi, L., et al. (2007). Mars reconnaissance orbiter's high resolution imaging science experiment (hirise). *Journal of Geophysical Research: Planets*, 112(E5).

Melosh, H. and Collins, G. (2005). Planetary science: Meteor crater formed by low-velocity impact. *Nature*, 434(7030):157.

Melosh, H. and Ivanov, B. (1999). Impact crater collapse. *Annual Review of Earth and Planetary Sciences*, 27(1):385–415.

Melosh, H., Ryan, E., and Asphaug, E. (1992). Dynamic fragmentation in impacts: Hydrocode simulation of laboratory impacts. *Journal of Geophysical Research: Planets*, 97(E9):14735–14759.

Melosh, H. J. (1979). Acoustic fluidization: A new geologic process? *Journal of Geophysical Research: Solid Earth*, 84(B13):7513–7520.

Melosh, H. J. (1989). Impact cratering: A geologic process. *Research supported by NASA. New York, Oxford University Press (Oxford Monographs on Geology and Geophysics, No. 11), 1989, 253 p.*, 11.

Melosh, H. J. (2011). *Impact cratering*, page 222–275. Cambridge Planetary Science. Cambridge University Press.

Melosh, H. J. (2013). The contact and compression stage of impact cratering. *Impact Cratering: processes and products*, pages 32–42.

Michael, G. and Neukum, G. (2010). Planetary surface dating from crater size–frequency distribution measurements: Partial resurfacing events and statistical age uncertainty. *Earth and Planetary Science Letters*, 294(3-4):223–229.

Michael, G., Platz, T., Kneissl, T., and Schmedemann, N. (2012). Planetary surface dating from crater size–frequency distribution measurements: Spatial randomness and clustering. *Icarus*, 218(1):169–177.

Morbidelli, A., Marchi, S., Bottke, W. F., and Kring, D. A. (2012). A sawtooth-like timeline for the first billion years of lunar bombardment. *Earth and Planetary Science Letters*, 355:144–151.

Murray, J. B., Muller, J.-P., Neukum, G., Werner, S. C., van Gasselt, S., Hauber, E., Markiewicz, W. J., Head III, J. W., Foing, B. H., Page, D., et al. (2005). Evidence from the mars express high resolution stereo camera for a frozen sea close to mars' equator. *Nature*, 434(7031):352.

Neukum, G. (1983). *Meteoritenbombardement und Datierung planetarer Oberflächen (German original). Meteorite bombardment and dating of planetary surfaces (English translation, 1984)*. PhD thesis, Habilitation Thesis for Faculty Membership, University of Munich.

Neukum, G. and Hiller, K. (1981). Martian ages. *Journal of Geophysical Research: Solid Earth*, 86(B4):3097–3121.

Neukum, G. and Ivanov, B. (1994). Crater size distributions and impact probabilities on earth from lunar, terrestrial-planet, and asteroid cratering data. *Hazards due to Comets and Asteroids*, 1:359–416.

Neukum, G., Ivanov, B. A., and Hartmann, W. K. (2001). Cratering records in the inner solar system in relation to the lunar reference system. In *Chronology and evolution of Mars*, pages 55–86. Springer.

Neukum, G. and Wise, D. (1976). Mars- a standard crater curve and possible new time scale. *Science*, 194(4272):1381–1387.

Nowka, D., Wünnemann, K., Collins, G., and Elbeshausen, D. (2010). Scaling of impact crater formation on planetary surfaces. In *European Planetary Science Congress*, volume 5.

Ohnaka, M. (1995). A shear failure strength law of rock in the brittle-plastic transition regime. *Geophysical Research Letters*, 22(1):25–28.

Öpik, E. J. (1960). The frequency of crater diameters in mare imbrium. *The Astronomical Journal*, 65:55.

Osinski, G. R., Grieve, R. A. F., and Tornabene, L. L. (2013). Excavation and impact ejecta emplacement. *Impact Cratering: processes and products*, pages 43–59.

Osinski, G. R. and Pierazzo, E. (2013). Impact cratering: Processes and products. *Impact Cratering: processes and products*, pages 1–20.

Panning, M. P., Lognonné, P., Banerdt, W. B., Garcia, R., Golombek, M., Kedar, S., Knapmeyer-Endrun, B., Mocquet, A., Teanby, N. A., Tromp, J., et al. (2017). Planned products of the mars structure service for the insight mission to mars. *Space Science Reviews*, 211(1-4):611–650.

Piekutowski, A. (1977). Cratering mechanisms observed in laboratory-scale high-explosive experiments. In *Impact and Explosion Cratering: Planetary and Terrestrial Implications*, pages 67–102.

Pierazzo, E., Artemieva, N., Ivanov, B., et al. (2005). Starting conditions for hydrothermal systems underneath martian craters: Hydrocode modeling. *Large meteorite impacts III*, 443.

Pike, R. J. (1977). Size-dependence in the shape of fresh impact craters on the moon. In *Impact and explosion cratering: Planetary and terrestrial implications*, pages 489–509.

Pike, R. J. (1988). Geomorphology of impact craters on mercury. *Mercury, University of Arizona Press*, pages 165–273.

Potter, R. W. K. (2012). Numerical modelling of basin-scale impact crater formation.

Prieur, N. C., Rolf, T., Luther, R., Wünnemann, K., Xiao, Z., and Werner, S. C. (2017). The effect of target properties on transient crater scaling for simple craters. *Journal of Geophysical Research: Planets*, 122(8):1704–1726.

Prieur, N. C., Rolf, T., Wünnemann, K., and Werner, S. C. (2018). Formation of simple impact craters in layered targets: Implications for lunar crater morphology and regolith thickness. *Journal of Geophysical Research: Planets*, 123(6):1555–1578.

Robbins, S. J. (2017). A global lunar crater database, complete for craters 1 km, ii. In *48th Lunar and Planetary Science Conference, held*, pages 20–24.

Schmidt, R. (1980). Meteor crater: Energy of formation-implications of centrifuge scaling. In *Lunar and Planetary Science Conference Proceedings*, volume 11, pages 2099–2128.

Schmidt, R. M. and Housen, K. R. (1987). Some recent advances in the scaling of impact and explosion cratering. *International Journal of Impact Engineering*, 5(1-4):543–560.

Senft, L. E. and Stewart, S. T. (2007). Modeling impact cratering in layered surfaces. *Journal of Geophysical Research: Planets*, 112(E11).

Shoemaker, E. M. (1961). Interplanetary correlation of geologic time. *AAPG Bulletin*, 45(1):130–130.

Van der Bogert, C. H., Hiesinger, H., Dundas, C. M., Krüger, T., McEwen, A. S., Zanetti, M., and Robinson, M. S. (2017). Origin of discrepancies between crater size-frequency distributions of coeval lunar geologic units via target property contrasts. *Icarus*, 298:49–63.

Watters, W. A., Hundal, C. B., Radford, A., Collins, G. S., and Tornabene, L. L. (2017). Dependence of secondary crater characteristics on downrange distance: High-resolution morphometry and simulations. *Journal of Geophysical Research: Planets*, 122(8):1773–1800.

Werner, S. and Ivanov, B. (2015). Exogenic dynamics, cratering, and surface ages.

Werner, S. C. (2009). The global martian volcanic evolutionary history. *Icarus*, 201(1):44–68.

Werner, S. C., Ody, A., and Poulet, F. (2014). The source crater of martian shergottite meteorites. *Science*, 343(6177):1343–1346.

Wetherill, G. (1975). Late heavy bombardment of the moon and terrestrial planets. In *Lunar and Planetary Science Conference Proceedings*, volume 6, pages 1539–1561.

Williams, J.-P., Pathare, A. V., and Aharonson, O. (2014). The production of small primary craters on mars and the moon. *Icarus*, 235:23–36.

Williams, J.-P., van der Bogert, C. H., Pathare, A. V., Michael, G. G., Kirchoff, M. R., and Hiesinger, H. (2018). Dating very young planetary surfaces from crater statistics: A review of issues and challenges. *Meteoritics & Planetary Science*, 53(4):554–582.

Wünnemann, K., Collins, G., and Melosh, H. (2006). A strain-based porosity model for use in hydrocode simulations of impacts and implications for transient crater growth in porous targets. *Icarus*, 180(2):514–527.

Wünnemann, K., Nowka, D., Collins, G., Elbeshausen, D., and Bierhaus, M. (2011). Scaling of impact crater formation on planetary surfaces—insights from numerical modeling. In *Proceedings of the 11th hypervelocity impact symposium*, volume 20, pages 1–16. Fraunhofer Verlag.

Yang, J. and Kang, Z. (2019). Bayesian network-based extraction of lunar impact craters from optical images and dem data. *Advances in Space Research*.

Zel'dovich, Y. B. and Raizer, Y. P. (1967). Physics of shock waves and high-temperature hydrodynamic phenomena. 2:712–716.

Appendix A

Cumulative crater counting and slopes from numerical modelling

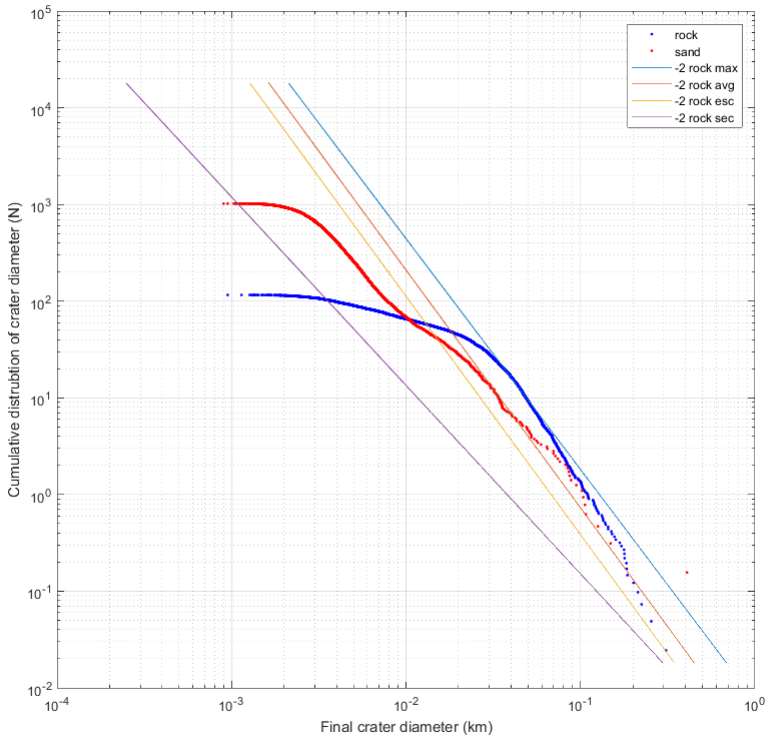

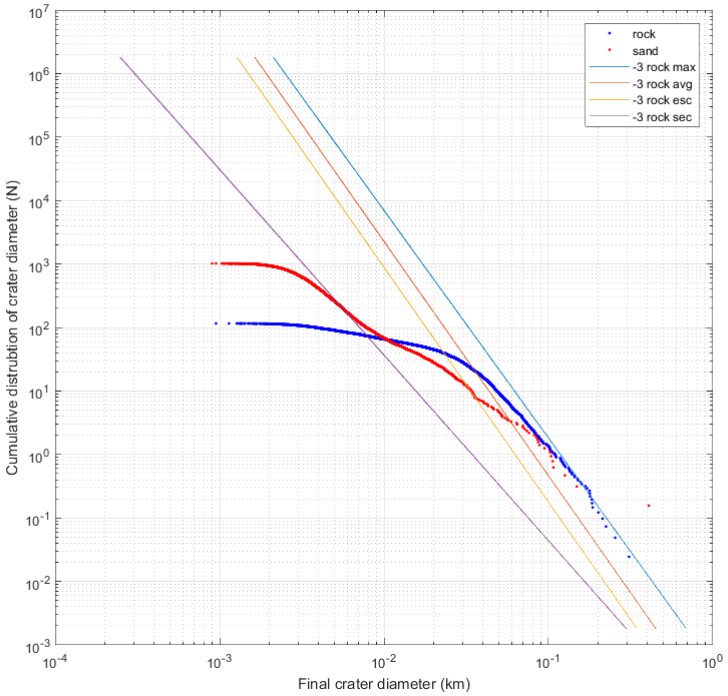
rock
sand
-3 rock max
-3 rock avg
-3 rock esc
-3 rock sec
Cumulative distrubtion of crater diameter (N)
Final crater diameter (km)

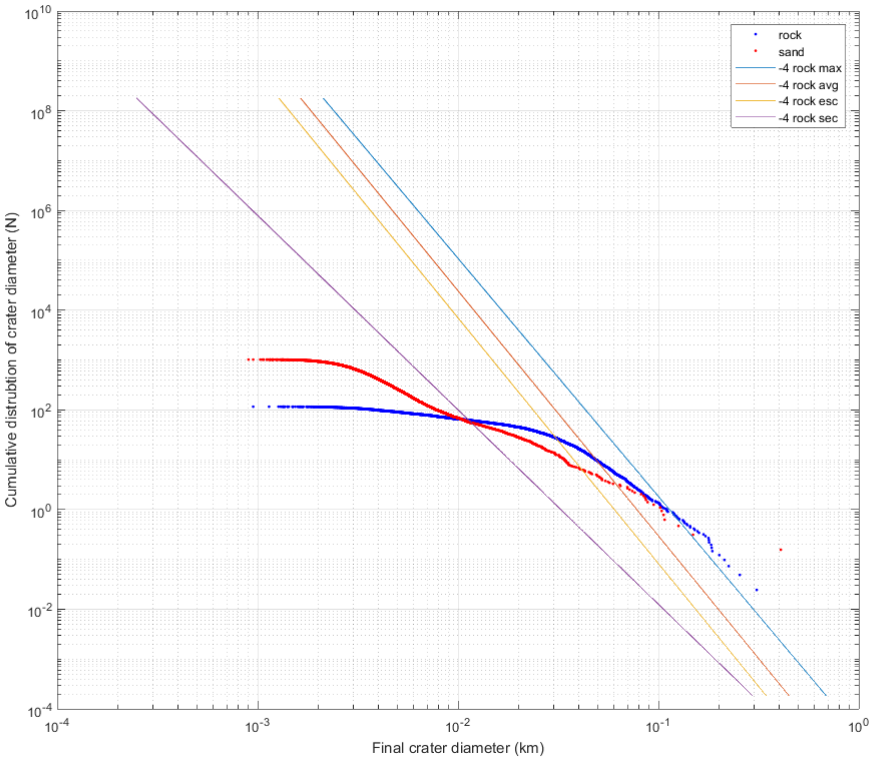
rock
sand
-4 rock max
-4 rock avg
-4 rock esc
-4 rock sec
Cumulative distrubtion of crater diameter (N)
Final crater diameter (km)

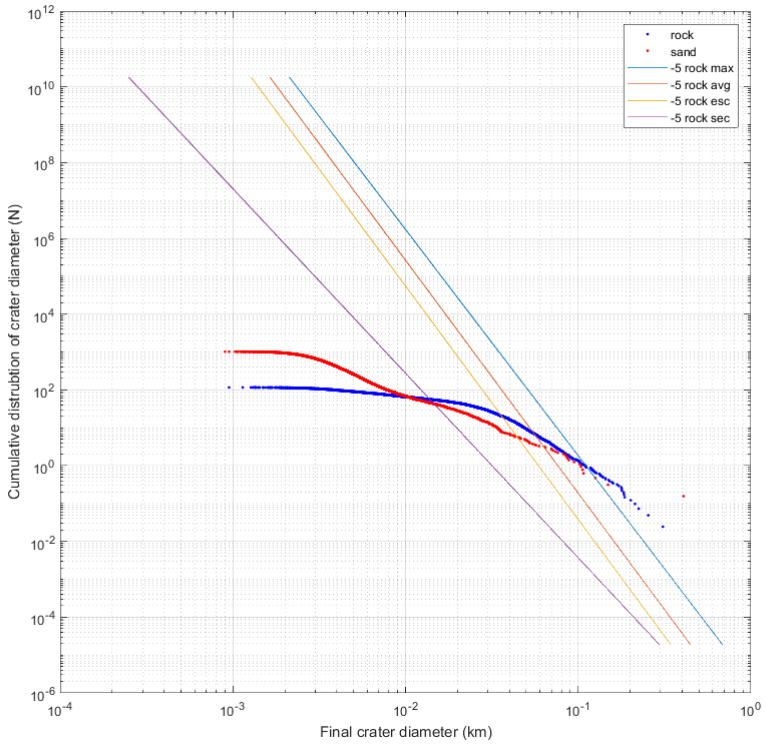
rock
sand
-5 rock max
-5 rock avg
-5 rock esc
-5 rock sec
Cumulative distrubtion of crater diameter (N)
Final crater diameter (km)

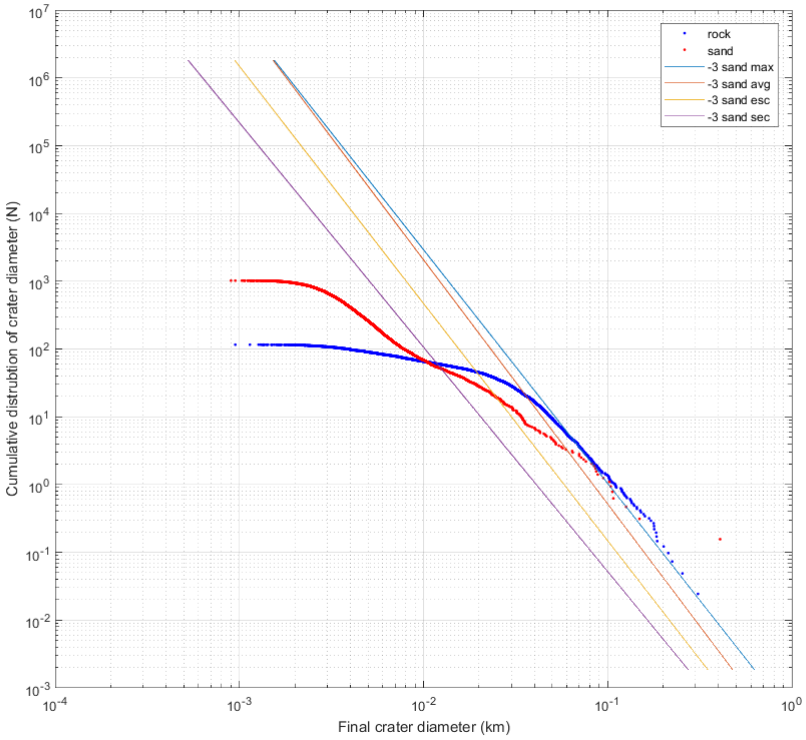
rock
sand
-3 sand max
-3 sand avg
-3 sand esc
-3 sand sec
Cumulative distrubtion of crater diameter (N)
Final crater diameter (km)

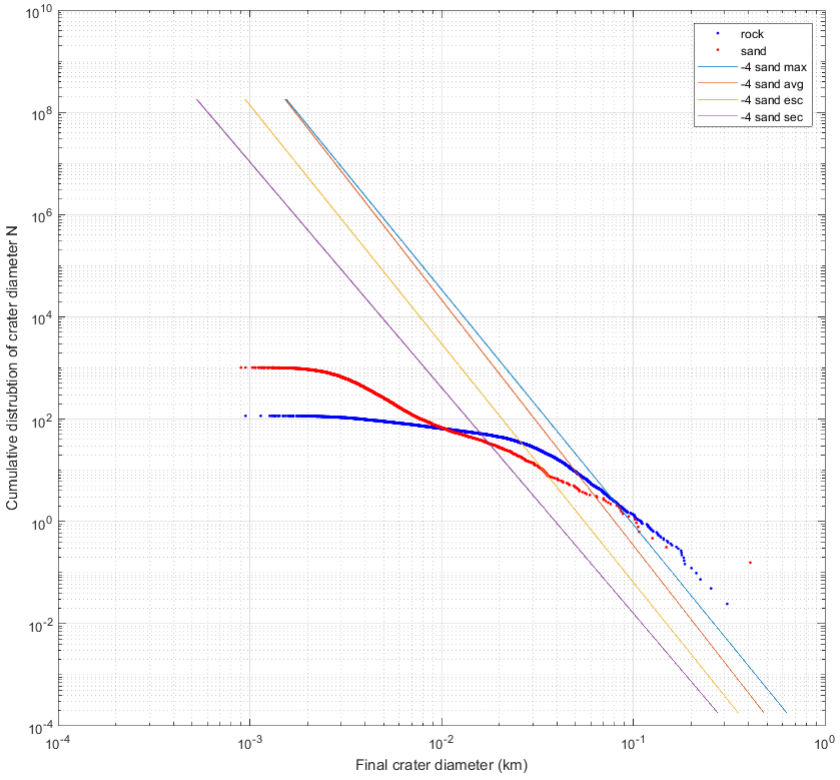
rock
sand
-4 sand max
-4 sand avg
-4 sand esc
-4 sand sec
Cumulative distrubtion of crater diameter N
Final crater diameter (km)

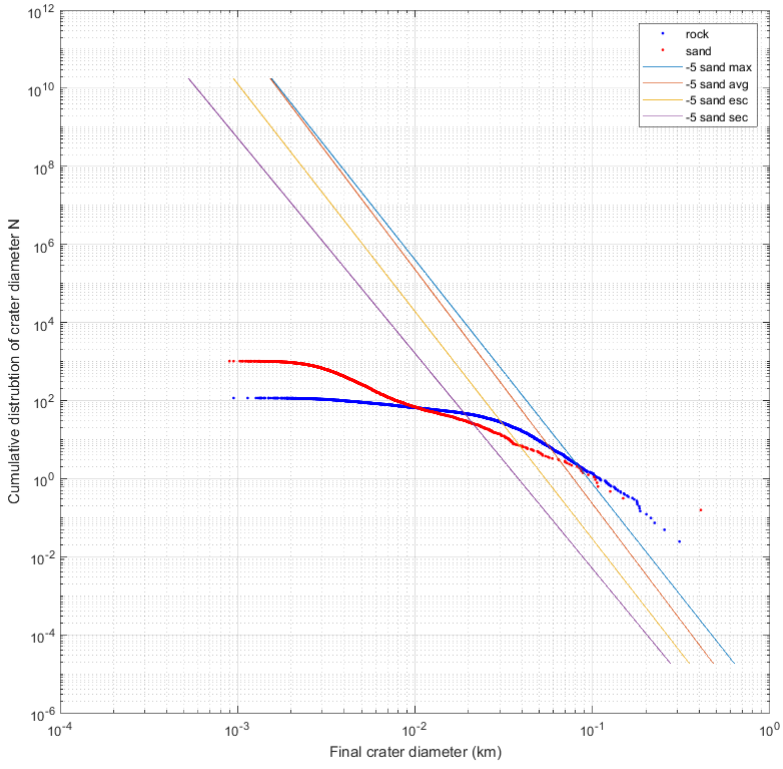
rock
sand
-5 sand max
-5 sand avg
-5 sand esc
-5 sand sec
Cumulative distrubtion of crater diameter N
Final crater diameter (km)